arXiv:1608.04332v2 [nucl-ex] 27 Sep 2016

Results of the ASY-EOS experiment at GSI: The symmetry energy at suprasaturation density

P. Russotto,[1] S. Gannon,[2] S. Kupny,[3] P. Lasko,[3] L. Acosta,[4,5] M. Adamczyk,[3] A. Al-Ajlan,[6] M. Al-Garawi,[7] S. Al-Homaidhi,[6] F. Amorini,[4] L. Auditore,[8,9] T. Aumann,[10,11] Y. Ayyad,[12] Z. Basrak,[13] J. Benlliure,[12] M. Boisjoli,[14] K. Boretzky,[11] J. Brzychczyk,[3] A. Budzanowski,[15,*] C. Caesar,[10] G. Cardella,[1] P. Cammarata,[16] Z. Chajecki,[17,18] M. Chartier,[2] A. Chbihi,[14] M. Colonna,[4] M. D. Cozma,[19] B. Czech,[15] E. De Filippo,[1] M. Di Toro,[4,20] M. Famiano,[18] I. Gašparić,[10,13] L. Grassi,[13] C. Guazzoni,[21,22] P. Guazzoni,[21,23] M. Heil,[11] L. Heilborn,[16] R. Introzzi,[24] T. Isobe,[25] K. Kezzar,[7] M. Kiš,[11] A. Krasznahorkay,[26] N. Kurz,[11] E. La Guidara,[1] G. Lanzalone,[4,27] A. Le Fèvre,[11] Y. Leifels,[11] R. C. Lemmon,[28] Q. F. Li,[29] I. Lombardo,[30,31] J. Łukasik,[15] W. G. Lynch,[17] P. Marini,[14,16,32] Z. Matthews,[2] L. May,[16] T. Minniti,[1] M. Mostazo,[12] A. Pagano,[1] E. V. Pagano,[4,20] M. Papa,[1] P. Pawłowski,[15] S. Pirrone,[1] G. Politi,[1,20] F. Porto,[4,20] W. Reviol,[33] F. Riccio,[21,22] F. Rizzo,[4,20] E. Rosato,[30,31,*] D. Rossi,[10,11] S. Santoro,[8,9] D. G. Sarantites,[33] H. Simon,[11] I. Skwirczynska,[15] Z. Sosin,[3,*] L. Stuhl,[26] W. Trautmann,[11] A. Trifirò,[8,9] M. Trimarchi,[8,9] M. B. Tsang,[17] G. Verde,[1,34] M. Veselsky,[35] M. Vigilante,[30,31] Yongjia Wang,[29] A. Wieloch,[3] P. Wigg,[2] J. Winkelbauer,[17] H. H. Wolter,[36] P. Wu,[2] S. Yennello,[16] P. Zambon,[21,22] L. Zetta,[21,23] and M. Zoric[13]

[1] *INFN-Sezione di Catania, I-95123 Catania, Italy*
[2] *University of Liverpool, Physics Department, Liverpool L69 7ZE, United Kingdom*
[3] *M. Smoluchowski Institute of Physics, Jagiellonian University, Pl-30-348 Kraków, Poland*
[4] *INFN-Laboratori Nazionali del Sud, I-95123 Catania, Italy*
[5] *Instituto de Física, Universidad Nacional Autónoma de México, A.P. 20-364, México 01000 D.F., Mexico*
[6] *KACST, Riyadh, Saudi Arabia*
[7] *Physics Department, King Saud University, Riyadh, Saudi Arabia*
[8] *INFN-Gruppo Collegato di Messina, I-98166 Messina, Italy*
[9] *Dipartimento di Scienze Matematiche e Informatiche, Scienze Fisiche e Scienze della Terra, University of Messina, I-98166 Messina, Italy*
[10] *Technische Universität Darmstadt, D-64289 Darmstadt, Germany*
[11] *GSI Helmholtzzentrum für Schwerionenforschung GmbH, D-64291 Darmstadt, Germany*
[12] *Universidade de Santiago de Compostela, 15782 Santiago de Compostela, Spain*
[13] *Ruđer Bošković Institute, HR-10002 Zagreb, Croatia*
[14] *GANIL, CEA et IN2P3-CNRS, F-14076 Caen, France*
[15] *H. Niewodniczański Institute of Nuclear Physics, Pl-31342 Kraków, Poland*
[16] *Department of Chemistry and Cyclotron Institute, Texas A&M University, College Station, TX-77843, USA*
[17] *Department of Physics and Astronomy and NSCL, Michigan State University, East Lansing, MI-48824, USA*
[18] *Western Michigan University, Kalamazoo, MI-49008, USA*
[19] *IFIN-HH, Reactorului 30, 077125 Măgurele-Bucharest, Romania*
[20] *Dipartimento di Fisica e Astronomia-Università, I-95123 Catania, Italy*
[21] *INFN-Sezione di Milano, I-20133 Milano, Italy*
[22] *Dipartimento di Elettronica, Informazione e Bioingegneria, Politecnico di Milano, I-20133 Milano, Italy*
[23] *Dipartimento di Fisica, Università degli Studi di Milano, I-20133 Milano, Italy*
[24] *INFN and DISAT, Politecnico di Torino, I-10129 Torino, Italy*
[25] *RIKEN, Wako, Saitama 351-0198, Japan*
[26] *Institute for Nuclear Research (MTA Atomki), P.O. Box 51, H-4001 Debrecen, Hungary*
[27] *Università degli Studi di Enna "Kore", I-94100 Enna, Italy*
[28] *STFC Daresbury Laboratory, Warrington WA4 4AD, United Kingdom*
[29] *School of Science, Huzhou University, Huzhou 313000, P.R. China*
[30] *INFN-Sezione di Napoli, I-80126 Napoli, Italy*
[31] *Dipartimento di Fisica "Ettore Pancini", Università di Napoli Federico II, I-80126 Napoli, Italy*
[32] *CENBGn Université de Bordeaux, CNRS/IN2P3, F-33175 Gradignan, France*
[33] *Chemistry Department, Washington University, St. Louis, MO-63130, USA*
[34] *Institut de Physique Nucléaire, IN2P3-CNRS et Université Paris-Sud, F-91406 Orsay, France*
[35] *Institute of Physics, Slovak Academy of Sciences, 84511 Bratislava 45, Slovakia*
[36] *Fakultät für Physik, Universität München, D-85748 Garching, Germany*

(Dated: September 28, 2016)

Directed and elliptic flows of neutrons and light charged particles were measured for the reaction ^{197}Au+^{197}Au at 400 MeV/nucleon incident energy within the ASY-EOS experimental campaign at the GSI laboratory. The detection system consisted of the Large Area Neutron Detector LAND, combined with parts of the CHIMERA multidetector, of the ALADIN Time-of-flight Wall, and of the Washington-University Microball detector. The latter three arrays were used for the event characterization and reaction-plane reconstruction. In addition, an array of triple telescopes, KRATTA,

was used for complementary measurements of the isotopic composition and flows of light charged particles.

From the comparison of the elliptic flow ratio of neutrons with respect to charged particles with UrQMD predictions, a value $\gamma = 0.72 \pm 0.19$ is obtained for the power-law coefficient describing the density dependence of the potential part in the parametrization of the symmetry energy. It represents a new and more stringent constraint for the regime of suprasaturation density and confirms, with a considerably smaller uncertainty, the moderately soft to linear density dependence deduced from the earlier FOPI-LAND data. The densities probed are shown to reach beyond twice saturation.

PACS numbers: 21.65.Cd, 21.65.Ef, 25.75.Ld

I. INTRODUCTION

Differences in the collective emission properties of neutrons and protons in neutron-rich heavy-ion reactions at intermediate bombarding energies have been proposed as potential observables for the study of the equation of state of asymmetric nuclear matter [1–4]. Among them, the neutron-proton elliptic-flow ratio and difference have been shown to be sufficiently sensitive probes of the high-density behavior of the nuclear symmetry energy [5, 6]. The comparison of existing data from the FOPI-LAND experiment [7, 8] with calculations performed with the UrQMD transport model [9–11] suggested a moderately soft to linear symmetry term, characterized by a coefficient $\gamma = 0.9 \pm 0.4$ for the power-law parametrization of the density dependence of the potential part of the symmetry energy [5]. This result has excluded super-soft scenarios but suffers from the considerable statistical uncertainty of the experimental data.

The same data set was also compared to calculations performed with the QMD model originally developed in Tübingen [12, 13] and a constraint compatible with the UrQMD result was obtained [6, 14, 15]. In addition, a thorough study of the parameter dependence of the model predictions was performed to devise a route towards a model-independent constraint of the high-density symmetry energy. It showed that presently acceptable limits for the choice of parameters in the isoscalar part of the transport description cause uncertainties comparable with but not larger than those of the experimental FOPI-LAND data [14]. It was also found that different parametrizations of the isovector part of the equation of state, the Gogny-inspired (momentum-dependent, Ref. [16]) and the power-law (momentum-independent) potential, lead to very similar predictions for the neutron-vs-charged-particle elliptic-flow ratio or difference.

To improve the statistical accuracy of the experimental flow parameters for the ^{197}Au+^{197}Au reaction and to extend the flow measurements to other systems, the symmetric collision systems ^{197}Au+^{197}Au, ^{96}Zr+^{96}Zr, and ^{96}Ru+^{96}Ru at 400 MeV/nucleon incident energies have been chosen for the asymmetric-matter equation-of-state (ASY-EOS) experimental campaign, conducted at the GSI laboratory in May 2011 (experiment S394). As in the FOPI-LAND experiment, the Large Area Neutron Detector (LAND) [17] was used for the detection and identification of neutrons and light charged particles. Parts of the CHIMERA multidetector [18, 19], of the ALADIN Time-of-flight Wall [20], and of the Washington University Microball detector [21] were used for the event characterization and determination of the azimuthal reaction-plane orientation. By including the Kraków Triple Telescope Array (KRATTA) [22] with isotopic identification of charged-particles up to atomic number $Z = 4$ in the setup, additional observables as, e.g., yields and flows of light-charged particles and yield ratios of the isobar pairs ^{3}H/^{3}He or ^{7}Li/^{7}Be were made available for the study of isospin effects in these reactions.

The results reported here refer exclusively to the ^{197}Au+^{197}Au reaction whose analysis has been completed. It is shown that the new data confirm the moderately soft to linear density dependence of the symmetry energy deduced from the earlier FOPI-LAND data. However, for technical reasons, the capabilities of the LAND detector could not be fully exploited. This had the effect that the originally intended measurement of detailed dependencies of the neutron flows on rapidity, transverse momentum, and particle type could not be fully realized. Uncertainties of some of the required corrections restricted the analysis to essentially only providing the ratio of neutron over charged-particle flows, integrated over the LAND acceptance. By comparing it with the results of UrQMD calculations adapted to the experimental acceptance and analysis conditions, a new and more stringent constraint for the symmetry energy at suprasaturation densities was derived.

The technical deficiencies of the LAND timing system, the methods developed to correct for them in the analysis, and the consequences for the obtained results are described and explained in detail in the Appendix. The confidence in the validity of the main, acceptance integrated, result is derived from the fact that it is found to be only weakly dependent on assumptions regarding details of the corrections. These uncertainties were quantitatively assessed by varying the assumptions within well-defined intervals and by treating their effects as systematic errors. These systematic and the statistical errors of the collected data set are of approximately equal magnitude.

*deceased

The present work derives its importance also from the fact that the flow probe, at present, appears to be the most robust observable for testing the nuclear equation of state at high densities. The recent comprehensive study of charged-particle flows for ^{197}Au+^{197}Au collisions at energies from 0.4 to 1.5 GeV/nucleon reflects a remarkable consistency in its support of a soft solution for the equation of state of symmetric matter, including momentum-dependent forces [23, 24]. It provides a narrower constraint than previously available [25]. Such narrower limits for the compressibility of symmetric nuclear matter are very useful also with regard to the equation of state of asymmetric matter. They have the effect of reducing systematic uncertainties originating from the choice of parameters for the isoscalar sector of a transport description [14].

Major efforts have recently been made to reduce the apparent systematic discrepancies in the interpretation of the FOPI pion ratios [26] with increasingly complex transport calculations [27–32]. Of particular interest is the observation that the predicted π^-/π^+ yield ratios are expected to rise when the medium modifications of pion production thresholds are explicitly considered [28]. This effect may permit reproducing the experimental values with choices for the symmetry energy that are less extreme than those required in some of the earlier pion studies [33–35]. However, the calculations of Hong and Danielewicz [27] exhibit only a small sensitivity of integrated pion ratios to the stiffness of the symmetry energy, pointing to the need for energy-differential observables. Further work will thus be required before pion yields and yield ratios can be reliably applied to the investigation of the high-density symmetry energy.

The important role played by the nuclear symmetry energy in nuclear structure and reactions as well as in astrophysics is the subject of several review articles [36–40]. A brief introductory review of the situation at suprasaturation densities is available in Ref. [41]. A comprehensive list of pertinent articles has recently appeared in Topical Issue on Nuclear Symmetry Energy [42].

II. EXPERIMENTAL DETAILS

A. Setup for S394

A schematic view of the experimental setup of the ASY-EOS experiment at the GSI laboratory is shown in Fig. 1. The beam was guided in vacuum to about 2 m upstream from the target. A thin plastic scintillator foil viewed by two photomultipliers was used to record the projectile arrival times and to serve as a start detector for the time-of-flight measurement. The Large Area Neutron Detector, LAND [17], was positioned to cover laboratory angles around 45° with respect to the beam direction. A veto wall of plastic scintillators in front of LAND allowed discriminating between neutrons and charged particles. In this configuration, it was possible to measure the directed and elliptic flows of neutrons and charged particles near midrapidity within the same angular acceptance. Opposite of LAND, covering a comparable range of polar angles, the Kraków Triple Telescope Array, KRATTA [22], had been installed to permit flow measurements of identified charged particles under the same experimental conditions. Results obtained with KRATTA will be published separately.

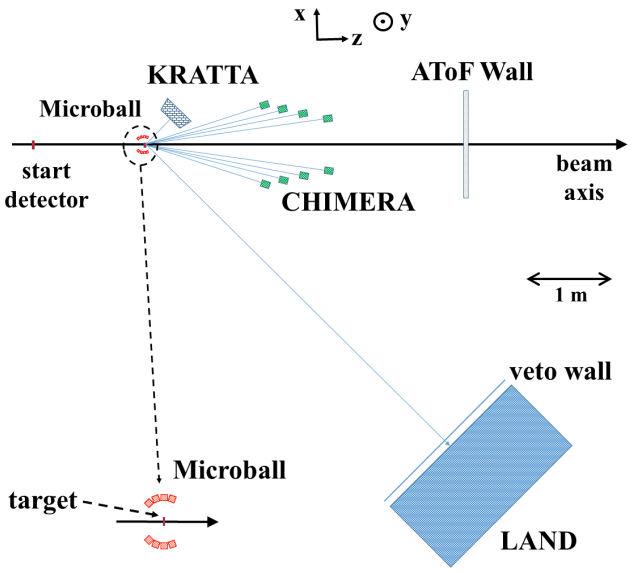

FIG. 1: Schematic view of the experimental setup of the ASY-EOS experiment S394 at GSI. The chosen coordinate system is indicated; the y direction points upwards in the laboratory. The target area with the Microball is not to scale in the main drawing but shown with a scale factor of approximately 5:1 in the lower left corner (see Sec. II B for coverage and dimensions).

For the event characterization and for measuring the orientation of the reaction plane, three detection systems had been installed. The ALADIN Time-of-Flight (AToF) Wall [20] was used to detect charged particles and fragments in the forward direction at polar angles up to $\theta_{\rm lab} \leq 7°$. Its capability of identifying large fragments and of characterizing events with a measurement of $Z_{\rm bound}$ [20] permitted the sorting of events according to impact parameter. Four double rings of the CHIMERA multidetector [18, 19] carrying together 352 CsI(Tl) scintillators in the forward direction and four rings with 50 thin CsI(Tl) elements of the Washington University Microball array [21] surrounding the target provided sufficient coverage and granularity for determining the orientation of the reaction plane from the measured azimuthal particle distributions.

The kinematic coverage achieved with this assembly of detection systems is illustrated in Figs. 2 and 3. In Fig. 3, in particular, the enhanced particle yields in the kinematic regimes of participant and spectator emissions are clearly visible. The product yields from the decay of the projectile spectator seen with CHIMERA and the

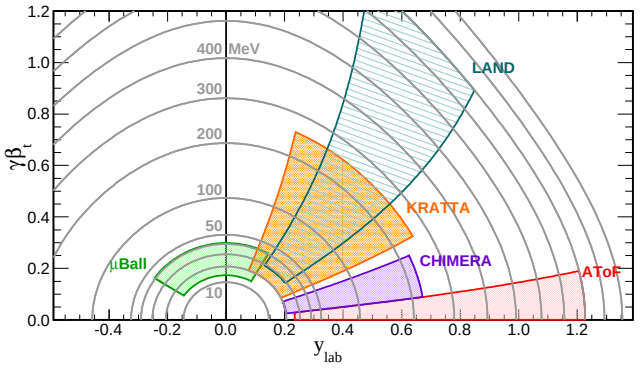

FIG. 2: Kinematic acceptance in the transverse-velocity vs rapidity plane of the detector systems used in the S394 experiment. The contour lines refer to the specified values of the kinetic energy of protons in the laboratory, ranging from 10 MeV to 1 GeV. The indicated lower and upper limits in energy are for protons (stopped protons for KRATTA and CHIMERA) and were calculated for the specific detector thresholds and configurations. An average value was chosen for the four types of detector elements of the Microball (labeled μBall in the figure).

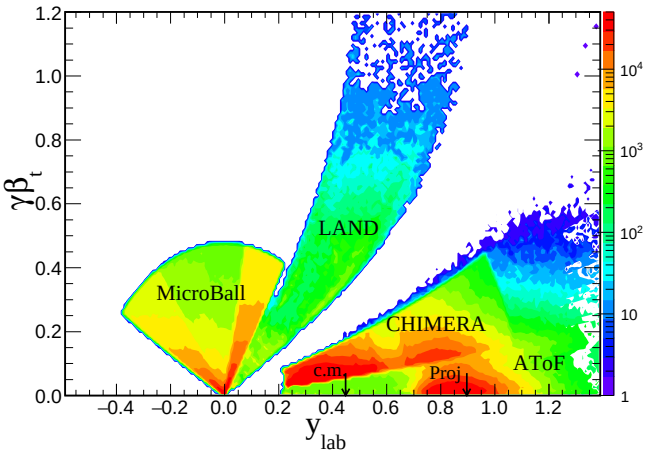

FIG. 3: Measured invariant hit distribution for ^{197}Au+^{197}Au collisions at 400 MeV/nucleon incident energy in the transverse-velocity vs rapidity plane for charged particles detected with the three systems Microball, CHIMERA, and AToF Wall with full azimuthal coverage and for neutrons detected with LAND. The velocities of particles detected with the Microball are not measured and shown here with an arbitrarily chosen homogeneous kinetic-energy distribution in the interval $0 \leq E_{\rm kin} \leq 100 MeV$. The apparent angular variation may be influenced by ring-dependent thresholds. The arrows indicate the rapidities of the projectile $y_p = 0.896$ and of the c.m. system.

AToF Wall do not exactly match because the AToF efficiency for hydrogen isotopes in this energy range is lower than that of the CHIMERA modules.

B. Detection systems

1. *LAND detector*

The Large Area Neutron Detector, LAND [17], upgraded with new TACQUILA electronics developed at GSI [43], was positioned at a distance of 5 m from the target. Its kinematic acceptance was similar to that of the forward LAND subdetector used in the FOPI-LAND experiment [5] but slightly larger in rapidity for given transverse momentum owing to the shorter distance from the target. LAND consists of 10 consecutive layers of 2×2 m^2 area, together adding up to the 1-m depth of the detector. Each layer is formed by 20 modules of 2-m length whose orientations alternate from layer to layer between vertical and horizontal. The modules have a 10×10 cm^2 cross section and are built from nine sheets of iron and ten sheets of plastic-scintillator material, all 5 mm thick, arranged in alternating order and oriented parallel to the entrance plane of the detector. Two iron sheets of 2.5 mm thickness form the entrance and exit layers of each module. In this design, the iron serves as a converter and the plastic scintillators as detectors for the produced ionizing radiation.

As it turned out during the analysis, the standard method of identifying the showers generated by interacting neutrons in the full LAND assembly was not feasible because of the timing difficulties related to the use of the new electronic system (discussed in Sec. III A below and in the Appendix). Only 19 modules (out of 20) of the first layer of LAND are included in the present analysis. This lowers the detection efficiency for neutrons and modifies its energy dependence, effects that had to be taken into account. The resulting range of polar angles that were covered by this part of LAND was $37.7^\circ \leq \theta_{\rm lab} \leq 56.5^\circ$ with respect to the beam direction.

A veto wall consisting of 10-cm-wide and 5-mm-thick plastic-scintillator slabs covered the front face of LAND, permitting the distinction between neutral and charged particles. The slabs were mounted in vertical orientation parallel to the modules of the first plane of LAND. Charged particles were identified on the basis of coincident hits in the veto wall, matching the time and position of the corresponding hit in LAND. However, owing to insufficient resolution achieved in the readout of the analog signals, the identification of the atomic number Z of the recorded charged particles on the basis of their energy loss in the veto-wall scintillators was not feasible. The comparative analysis was thus restricted to the collective flows of neutrons with respect to that observed for all charged particles detected within the acceptance of LAND.

2. *KRATTA hodoscope*

The Kraków Triple Telescope Array, KRATTA [22], was specifically designed for the experiment to measure

the energy, emission angles, and isotopic composition of light charged reaction products. The 35 modules of KRATTA were arranged in a 7×5 array and placed opposite to LAND at a distance of 40 cm from the target. They covered 160 msr of solid angle at polar angles between 24° and 68°. The modules of KRATTA consisted of two, optically decoupled, CsI(Tl) crystals (thickness of 2.5 and 12.5 cm) and three large-area, 500-μm-thick, PIN photodiodes. The middle photodiode and the short CsI(Tl) crystal read out by the diode from its front face were operated as a single-chip telescope [44]. Very good isotopic resolution has been obtained in the whole dynamic range up to $Z \sim 4$. The methods used for deriving it and the virtue of using digital pulse-shape recording throughout are described in Ref. [22].

3. *CHIMERA hodoscope*

Four double rings of the CHIMERA multidetector [18, 19] had been transported to the GSI laboratory and installed at their nominal distances from the target, covering polar angles between 7° and 20°. They carried together 352 CsI(Tl) scintillators, 12 cm in thickness and read out with photodiodes. Each of the eight individual rings provided a 2π azimuthal coverage with either 40 or 48 modules per ring. For calibration purposes, four of the Si detectors of the regular CHIMERA setup were installed in each ring. For these telescopes, an independent digital pulse-shape acquisition system was used to investigate and improve the particle identification and calibration methods [45]. The recorded telescope data proved very useful for verifying the analysis schemes developed for this experiment.

The CHIMERA rings were intended for the detection and identification of light-charged particles, primarily expected to come from the midrapidity regime. In the analysis, a rapidity gate $y > 0.1$ in the center-of-mass (c.m.) reference system was applied to exclusively select forward-hemisphere emissions for determining the orientation of the reaction plane.

For the use of CHIMERA modules at the present energy regime, the identification of punch-through particles was essential. In addition, the velocity of registered particles had to be reconstructed with an accuracy permitting the application of the rapidity gate. For particles stopped in the CsI, this was done using the mass number A and the deposited energy of the particles resolved in the fast-vs-slow identification map.

For particles punching through the CsI, their atomic number, essentially $Z = 1$ or 2, was evident in the fast-vs-slow identification plots. A most probable mass number A was assigned on the basis of the measured energy loss ΔE and used to reconstruct the total kinetic energy and momentum. The mass $A = 4$ was assigned to helium isotopes. In the case of the hydrogen isotopes, $A = 3$ was assigned to a $Z = 1$ particle if $\Delta E_d^{p.t.} < \Delta E < \Delta E_t^{p.t.}$, $A = 2$ was assigned if $\Delta E_p^{p.t.} < \Delta E < \Delta E_d^{p.t.}$, and $A = 1$ was assigned if $\Delta E < \Delta E_p^{p.t.}$. Here $\Delta E_x^{p.t.}$ refers to the calculated maximum energy loss ΔE deposited in the CsI(Tl) module by punch-through particles, and the subscript $x = p, d, t$ indicates protons, deuterons and tritons, respectively. The reconstructed total kinetic energy was then used to determine the velocity of the particle. An example of the two-dimensional maps used for the particle identification and analysis is shown in Fig. 4.

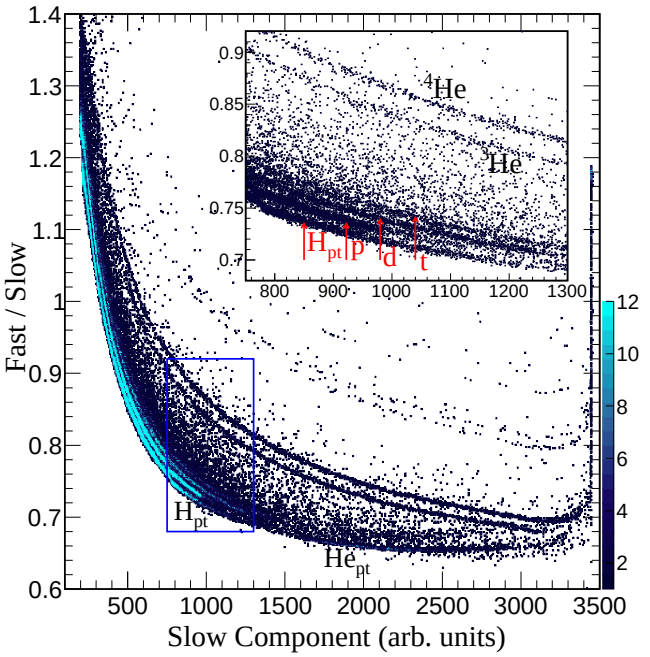

FIG. 4: Identification plot of CsI(Tl) signals recorded with a CHIMERA module of ring 7 ($\theta_{\rm lab} \approx 17°$) from ^{197}Au+^{197}Au collisions at 400 MeV/nucleon displaying the ratio of fast-over-slow vs the slow signal components. The loci of hydrogen and helium ions punching through the full length of the detector are labeled as H_{pt} and He_{pt}. An expanded view of the area within the rectangular box is shown in the inset. Besides the punch-through groups, also the loci of mass-identified light ions are indicated there.

4. *ALADIN ToF Wall*

A central square part of the ALADIN Time-of-Flight (AToF) Wall [20] with an area of approximately 1 m^2 was placed symmetrically with respect to the beam direction at a distance of 3.7 m downstream from the target. It was used to detect forward emitted charged particles and fragments at polar angles smaller than 7°, i.e. within the opening of the forward-most CHIMERA ring. The two layers of the AToF Wall (front and rear) each consisted of 48 modules of 2.5×110 cm^2 plastic scintillators with a thickness of 1 cm and with photomultipliers mounted at their upper and lower end faces. The modules are arranged in densely packed groups of eight modules, six groups per layer, and all oriented in vertical direction.

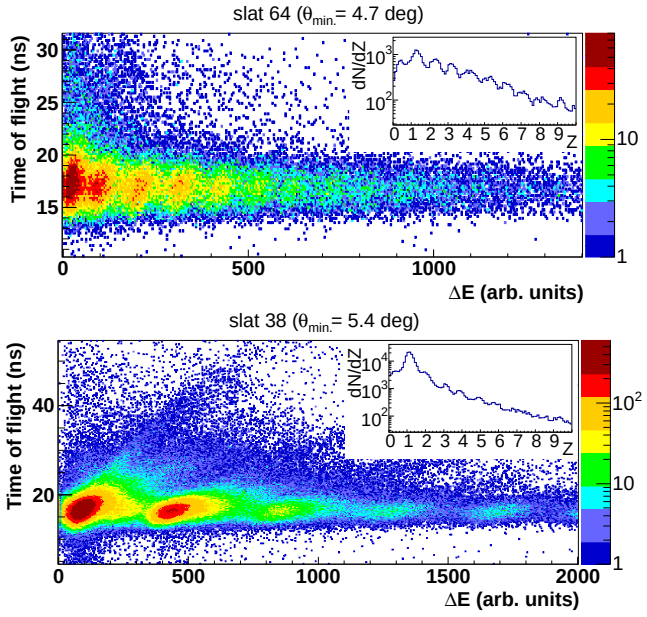

FIG. 5: AToF identification plots of calibrated time of flight vs recorded energy loss ΔE for two slats approximately 30 and 35 cm to the right of the beam direction ($\theta_{\rm lab} \approx 4.7^\circ$ and $\approx 5.4^\circ$, respectively, at their central parts). The groups of light elements are clearly recognized up to atomic number $Z \approx 10$ as shown in the insets on logarithmic scales.

They provided the atomic numbers Z of the detected fragments and light charged particles, as well as their velocities and directions of emission. The threshold was set below the maximum of the $Z = 1$ distribution in the spectrum of recorded energy-loss signals. A central hole of 7.5×7.5 cm^2 permitted the non-interacting beam to pass undetected through the AToF Wall.

The atomic number Z of light fragments is individually resolved on the basis of the measured time and energy loss up to approximately $Z = 10$, as illustrated in Fig. 5. The unusually high background appearing in these maps is attributed to interactions of the ions with air during their flight path to the detector. Heavier fragments are identified with a resolution of $\Delta Z \approx 2$ (FWHM) on the basis of the Z calibrations generated in earlier experiments with the AToF Wall [20, 46]. The time-of-flight resolution varies with Z, smoothly decreasing from 300 ps (standard deviation) for lithium fragments to about 100 ps for fragments with $Z > 10$. The AToF timing signals were used to generate a reaction trigger. The minimum requirement was three recorded tracks in the front-wall modules and three recorded tracks in the rear-wall modules. The front- and rear-wall tracks are usually pairwise correlated and produced by the same particles. The central group of eight modules containing the central opening was not included in the trigger circuit. These trigger requirements had the effect of suppressing collisions producing moderate excitations. However, the forward position of the wall and the long passage of the beam through air had the effect of still producing unwanted trigger signals generated by reactions on non-target material. The methods chosen to efficiently eliminate such events in the analysis are explained below.

5. *Microball*

The target was surrounded by an array of 50 3.6-to-5.6-mm-thick CsI(Tl) elements of the Washington University Microball (so-called Reaction Microball [21]). This array had four azimuthally symmetric rings, subtended the range of polar angles between 60° and 147° in the laboratory, and thus was essentially sensitive to backward emissions in the c.m. frame of the reaction. The azimuthal distributions of modules recording a hit above threshold provided a measure of the orientation of the reaction plane as seen in the rear hemisphere. The small diameter of the array of only about 10 cm offered a nearly negligible solid angle for reactions occurring downstream from the target, a property that was used for suppressing background reactions in the analysis.

C. Beams and targets

With beam intensities of about 10^5 pps and targets of 1-2% interaction probability, about 5×10^6 events were collected for each of the systems ^{197}Au+^{197}Au, ^{96}Zr+^{96}Zr, and ^{96}Ru+^{96}Ru. Additional runs were performed without a target to measure the background from the interaction of projectile ions with non-target material. The 3.7 m column of air between the target and the AToF Wall represents by itself an additional target with a theoretical interaction probability of about 6% for ^{197}Au projectiles.

Measurements with iron shadow bars in front of LAND, with and without a target, were used to determine the background of scattered neutrons not directly originating from the target. The shadow bars consisted of several pieces of iron, together representing a block of 60 cm in thickness and shaped to precisely cover the solid-angle acceptance of the LAND detector as seen from the target position. Results obtained with the ^{96}Zr and ^{96}Ru beams and targets are not presented here.

III. DATA ANALYSIS

The analysis of the experimental data has been performed within the FairRoot software framework primarily developed for the use with the future Facility for Antiproton and Ion Research (FAIR) detectors [47]. The FairRoot framework contains a complete simulation of the ASY-EOS detector setup and geometry and of the data analysis schemes. Theoretical calculations can be performed within the same software environment and filtered to adapt them to the experimental acceptance and analysis conditions.

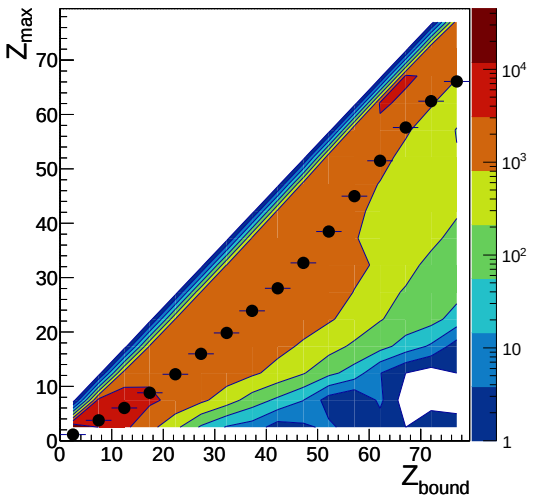

FIG. 6: Experimental correlation of the maximum atomic number, $Z_{\rm max}$, of the fragments within an event and the quantity $Z_{\rm bound}$ as deduced from the fragments detected with the AToF Wall. The dots represent the mean values of $Z_{\rm max}$ over the intervals of $Z_{\rm bound}$ indicated by the horizontal error bars.

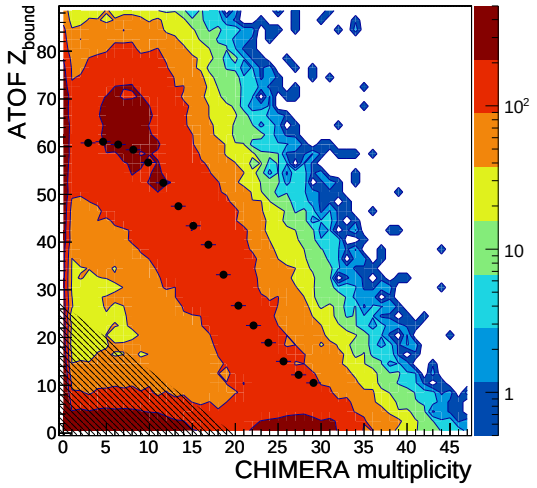

FIG. 7: Experimental correlation of the quantity $Z_{\rm bound}$ as deduced from the fragments detected with the AToF Wall with the charged-particle multiplicity measured with CHIMERA. Events within the hatched area were excluded from the analysis; the high-intensity group near multiplicity 27 with $Z_{\rm bound} \approx 0$ is caused by central collisions; the symbols represent the mean $Z_{\rm bound}$ of the remaining distribution as a function of the CHIMERA multiplicity.

A. LAND timing

A major difficulty arose from the fact that the new TACQUILA electronics [43] of the LAND detector did not permit the recognition of the very-low-energy γ-ray signals in the LAND modules. The absolute time calibration, therefore, had to be obtained from a spectra comparison with data of the FOPI-LAND experiment. Furthermore, the digital timing information was found to be frequently, with approximately 30% -40% probability, affected by $\pm$25 ns time jumps, arising from errors in counting the number of 25-ns clock cycles occurring between the start and the stop signals in a time measurement. These uncertainties were identified and corrected with procedures that are described in detail in the Appendix. Where possible, recourse was taken by comparing with or adjusting to existing data from previous FOPI and FOPI-LAND experiments.

The goal pursued in the present analysis consisted in applying the evident corrections and in quantifying the uncertainties associated with correction steps that could not be unambiguously determined. For the time-resolved differential data, the main uncertainty arises from the so-called second correction step, devised for wrongly recorded hits not recognized in the first correction step (see the Appendix). In addition to recovering the correct times of the intended class of hits, it has the side effect of misplacing an unknown number of valid hits in the time spectra. This causes a mixing of the flow properties within the affected time intervals. The problem was investigated by applying the second correction to randomly chosen fractions of the selected group of candidate hits and by comparing the consequences with data sets obtained in FOPI measurements [48]. It is shown that the mixing affects the deduced flow parameters but, to a much smaller extent, the flow ratios. Its contribution to the systematic error of the power-law exponent γ amounts to $\Delta\gamma = \pm 0.05$.

This particular correction and the mixing that it causes play only a minor role for the acceptance-integrated results obtained after integrating over the full time spectra. Timing errors have no consequence here as long as they do not lead beyond the limits of the integration interval. A remaining source of uncertainty is the precise choice of the low-energy thresholds as it should match their counterparts in the calculations. For charged particles, the threshold energy is given by the requirement to pass through the veto wall and to reach the first scintillator plane of LAND, for protons about 60 MeV. It is thus independent of the time measurement, provided the hit is within the accepted time interval. For neutrons, the low-energy threshold is defined by the chosen integration limit at long times-of-flight. Timing errors are effective here. To minimize the overall uncertainty, the integration limit was placed at times of flight much longer than expected for charged particles and into a low-intensity region less affected by the timing corrections (see the Appendix). Its nominal value corresponded to 30 MeV kinetic energy for nucleons. The level of remaining uncertainties was determined by varying the integration limit within a wide interval and by comparing with calculations performed with corresponding energy thresholds for neutrons. As observed in the differential case, the flow ratios are only mildly affected because uncertainties cancel. The observed variation of $\Delta\gamma = \pm 0.07$ represents the overall systematic error arising from the LAND tim-

ing properties.

B. Impact parameter determination

For selecting according to impact parameter, global variables were constructed from the CHIMERA and AToF data. They included

$$Z_{\rm bound} = \sum_{i=1}^{N} Z_i \text{ with } Z_i \geq 2 \quad (1)$$

and the ratio of transverse to longitudinal charge,

$$\text{ZRAT} = 10 Z_{\rm trans}/Z_{\rm long} \quad (2)$$

with an arbitrarily chosen scale factor 10 and with

$$Z_{\rm trans} = \sum_{i=1}^{N} Z_i sin^2(\theta_i),\ Z_{\rm long} = \sum_{i=1}^{N} Z_i cos^2(\theta_i) \quad (3)$$

where θ_i is the polar angle of the i^{th} particle in the laboratory reference system. $Z_{\rm bound}$ is close to the charge of the primary spectator system and monotonically correlated with the impact parameter, while ZRAT increases with the centrality of the reaction. The choice of these variables as impact parameter selectors has been guided by performing UrQMD calculations for given impact parameter ranges and filtering the simulated reaction events for angular acceptance, detection thresholds, and resolution of the detectors.

For constructing $Z_{\rm bound}$, fragments recorded with CHIMERA and the AToF Wall were used where not otherwise indicated. Larger fragments ($Z > 4$) are exclusively expected at very forward angles, well within the kinematic acceptance of $\theta_{\rm lab} \leq 7^\circ$ of the AToF Wall (cf. Figs. 4 and 5). The evolution of the largest atomic number, $Z_{\rm max}$, observed in an event as a function of $Z_{\rm bound}$, here from AToF alone, is shown in Fig. 6. The relative behavior of these two observables resembles closely that known from earlier results reported by the ALADIN Collaboration for the ^{197}Au+^{197}Au reaction [20, 49]. Only for large $Z_{\rm bound}$ is a difference observed, as $\langle Z_{\rm max} \rangle$ does not reach up as close to the projectile Z as it did in the ALADIN experiments with different trigger conditions. The trigger chosen for the present experiment suppressed the most peripheral events with a small multiplicity of charged particles and a corresponding $Z_{\rm max}$ near $Z = 79$.

The expected anticorrelation of $Z_{\rm bound}$ as determined from AToF alone, rising with impact parameter b and the multiplicity of charged particles measured with the CHIMERA rings at intermediate angles is observed as well (Fig. 7). The group of events with both small $Z_{\rm bound}$ and small multiplicities detected with CHIMERA (hatched area in the figure) is interpreted as containing nearly undeflected heavy projectile fragments that have passed undetected through the central hole of the AToF Wall. Such events are expected from very peripheral

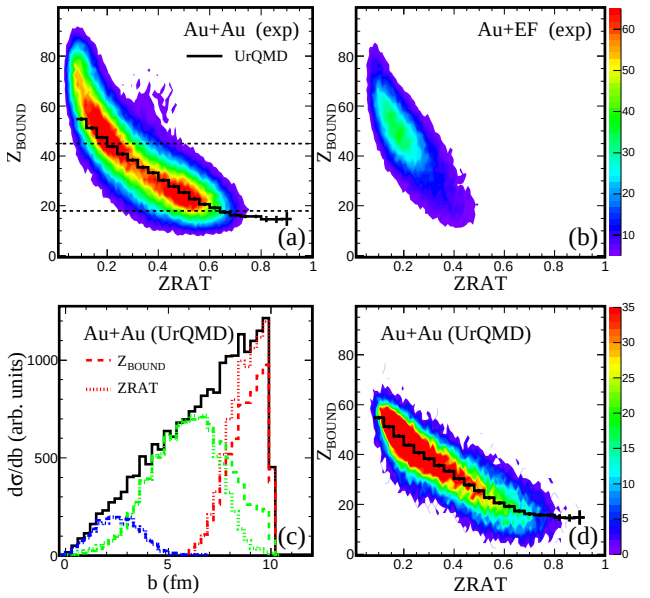

FIG. 8: (Top row) Inclusive $Z_{\rm bound}$ vs ZRAT correlation for data sets taken with (a) and without (b) a target foil in place (EF stands for empty frame).
(Bottom row) UrQMD calculations for the correlation of $Z_{\rm bound}$ vs ZRAT for ^{197}Au+^{197}Au collisions at 400 MeV/nucleon and impact parameter $b < 10.0$ fm, filtered to match the experimental conditions (d), and for impact-parameter distributions $d\sigma/db$ obtained under various conditions (c). The unbiased distribution for the full reaction for $b < 10.0$ fm is given by the black (solid) histogram while the blue, green, and red lines show impact parameter distributions obtained when selecting very central, semicentral, and peripheral event classes, respectively, by gating either on $Z_{\rm bound}$ (dashed) or on ZRAT (dotted, see Table I). The dashed horizontal lines in (a) represent the corresponding gates for the $Z_{\rm bound}$ selection. The line of $Z_{\rm bound}$ centroids as a function of ZRAT of the UrQMD distribution of (d) is drawn into the experimental distribution (a).

^{197}Au+^{197}Au collisions as well as from the interaction of the beam with N or O nuclei of the air downstream of the target. The class of events within the hatched region was not further considered in the analysis.

The correlation of $Z_{\rm bound}$ with ZRAT, as obtained from the combined CHIMERA and AToF data for ^{197}Au+^{197}Au collisions at 400 MeV/nucleon, are presented in Fig. 8 (a). The two impact-parameter sensitive quantities are globally anticorrelated as expected: $Z_{\rm bound}$ grows while ZRAT drops with increasing impact parameter. For orientation, ZRAT = 0.15 is obtained for particles detected at the forward limit of the CHIMERA acceptance $\theta_{\rm lab} = 7^\circ$, ZRAT = 1.3 for particles detected at the largest angle $\theta_{\rm lab} = 20^\circ$, and ZRAT $\approx$ 0.7 for a homogeneous distribution within the CHIMERA acceptance. The observed distribution is compatible with these limits. Values smaller than ZRAT = 0.15 are suppressed by the trigger condition of four or more charged particles detected with CHIMERA and two or more hits

recorded by the Microball by which peripheral collisions are suppressed. In addition, the adopted condition requiring an anticorrelation of the preferential azimuthal directions of these particles observed with CHIMERA and with the Microball was applied (see Sec. III D). A very similar pattern is observed for the result of UrQMD calculations, performed for the range of impact parameters $b < 10.0$ fm [Fig. 8(d)]. The centroid line deduced from the simulations follows the experimental distribution shown in panel (a) rather well.

The correlation observed when the target foil is removed is shown in panel (b) of Fig. 8. The yields are normalized with respect to the integrated beam intensity, so that the much lower intensity of background reactions becomes evident. They display a similar anticorrelation, however much less pronounced and extending mainly over the range typical for the more peripheral collisions in the ^{197}Au+^{197}Au case. The observed concentration of background events at large $Z_{\rm bound} > 40$ also coincides with the expectation for collisions of ^{197}Au beam particles with predominantly ^{14}N encountered downstream of the target location [50]. The initially high yield of AToF trigger signals from ^{197}Au+air collisions is reduced to the apparent low level by applying the conditions on the multiplicity and azimuthal orientation of Microball hits within the event.

Class, b interval	$Z_{\rm bound}$			ZRAT		
	min	max	$< b >$	min	max	$< b >$
very central, < 3.0 fm	0	18	2.56	0.615	2.0	2.51
semi-c, $3.0 - 7.5$ fm	18	45	6.18	0.245	0.615	5.71
peripheral, > 7.5 fm	45		8.74		0.245	8.76
central, < 7.5 fm	0	45	5.69	0.245	2.0	5.27
FOPI, $3.35 - 6.0$ fm	19	33	5.00	0.365	0.585	4.69

TABLE I: Selection gates used to define the indicated five classes of centrality. Their names and the nominal ranges of impact parameter b are given in the first column (semi-c stands for semicentral). The gate required for the comparison with FOPI data (Sec. IV A) is given in the bottom row. The following columns list the minimum and maximum values of the gating intervals used and the corresponding mean values of the impact parameter b as given by the UrQMD calculations for the two sorting variables $Z_{\rm bound}$ (columns 2-4) and ZRAT (columns 5-7). No upper gate of $Z_{\rm bound}$ and no lower gate of ZRAT was applied when selecting peripheral events.

For the actual impact-parameter selections within the range of interest $b < 7.5$ fm, the global observables $Z_{\rm bound}$ and ZRAT were used. The intervals chosen to select very central, semicentral and peripheral event classes are listed in Table I together with the mean impact parameters expected for these classes according to the UrQMD calculations. The condition on multiplicity specified above provided no additional restriction within this range of central and semicentral collisions [cf. Fig. 8(a)]. The quality of the resolution that can be expected, according to the UrQMD model, is illustrated in panel (c) of Fig. 8. The examples of very central, semicentral and peripheral selections with nominal impact-parameter intervals of $b < 3$ fm, $3 < b < 7.5$ fm, and $b > 7.5$ fm, respectively, are displayed. The expected smoothing of the boundaries of the actually selected intervals is about equal for the $Z_{\rm bound}$ and ZRAT observables. The interval chosen for generating the acceptance-integrated flow ratio in the final analysis is a nominal $b < 7.5$ fm, listed as central class in the table. As the calculations show, the actual distribution can be expected to contain nearly all events with $b < 6$ fm and, with decreasing probability, a selection of events with impact parameters up to $b \approx 10$ fm.

C. Reaction plane orientation

For the experimental estimates of the azimuthal orientation of the impact-parameter vector, both CHIMERA and AToF data were used. In the CHIMERA analysis, a Q vector [51] was calculated as

$$\vec{Q}_{\rm CHI} = \sum_{i=1}^{N} Z_i \vec{\beta_{t,i}} \gamma_i, \qquad (4)$$

with the transverse-velocity vectors $\vec{\beta_{t,i}}$ and with $N \geq 4$, i.e. by requiring at least four identified particles recorded by CHIMERA. An important factor in the Q-vector definition is the weight factor $\omega = +1(-1)$ for emissions in the forward (backward) hemisphere in the c.m. system. It is omitted here because emissions in the forward hemisphere are exclusively selected with the condition on rapidity $y_{c.m.} > 0.1$. The vector $\vec{Q}_{\rm CHI}$ represents a Z- and transverse-velocity-weighted, i.e. approximately transverse-momentum-weighted, direction in the plane perpendicular to the beam direction.

In the AToF analysis, a second vector $\vec{Q}_{\rm AToF}$ has been determined from the recorded positions of the interaction of detected fragments with the Time-of-Flight Wall. The horizontal coordinates were determined with the uncertainty given by the slat widths of 2.5 cm. It reduces to 1.25 cm if the fragment was identified in both layers as observed in most cases. The vertical coordinate was determined from the measured difference of the top and bottom time signals, and a resolution of typically about ± 2 cm was obtained. The distance to the beam axis, under the assumption of approximately beam velocity, is proportional to the transverse velocity of the detected particle or fragment. The resulting azimuthal vector was weighted with the atomic number Z of the fragment and $\vec{Q}_{\rm AToF}$ was obtained by summing over all individual vectors within an event. Also here, the weight factor ω can be omitted as the AToF acceptance of $\theta_{\rm lab} \leq 7^\circ$ strongly favors projectile fragments. A time-of-flight gate selecting forward emissions in the c.m. frame was used in addition.

The resolution obtained with these two quantities is overall comparable but depends somewhat on the impact parameter. Peripheral collisions associated with small

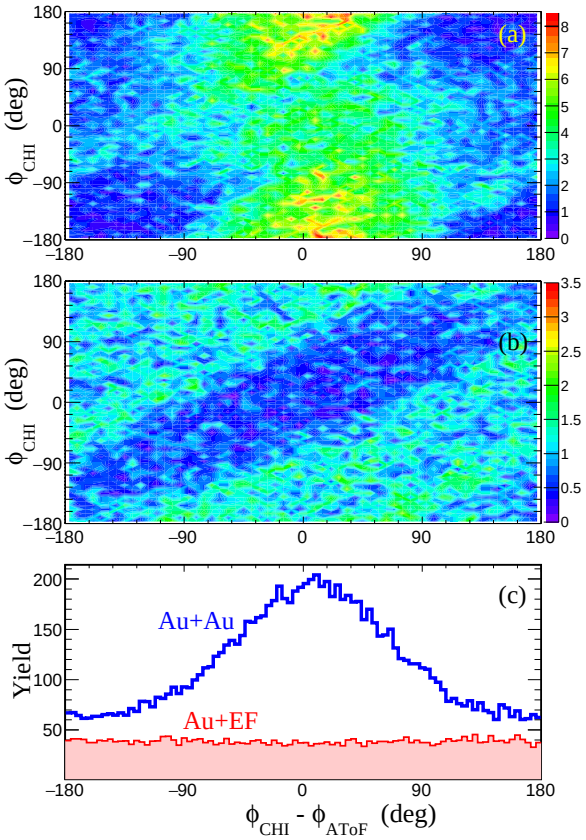

FIG. 9: Bidimensional representations of the difference of the azimuthal reaction-plane orientations individually obtained from CHIMERA and the AToF Wall, under the condition that the CHIMERA and Microball orientations are within the adopted anticorrelation gate and shown for measurements with (a) and without (b) a gold foil in the target frame. Panel (c) shows yield curves for these two cases, Au+Au and Au+EF (EF stands for empty frame), normalized with respect to the integrated beam intensity.

multiplicities in the CHIMERA part of the recorded event may be more easily characterized with the heavy fragments seen in AToF while more central collisions leading to high CHIMERA multiplicities may produce only few light fragments within the acceptance of the AToF Wall. As it turned out, in the impact parameter range of interest, central with $b \leq 7.5$ fm, only about 10% of the events permitted the calculation of a Q vector from AToF hits alone. Because the AToF geometry is not azimuthally symmetric, the resulting inclusive Q-vector distributions are not fully isotropic.

With the Microball data, the reaction-plane orientation was estimated by summing over the azimuthal directions of the recorded hits. A vector $\vec{Q}_{\mu\mathrm{Ball}}$ has been calculated as

$$\vec{Q}_{\mu\mathrm{Ball}} = \sum_{i=1}^{N} \hat{r}_t^i, \qquad (5)$$

where $\hat{r}_t^i$ is the azimuthal unit vector in the direction of

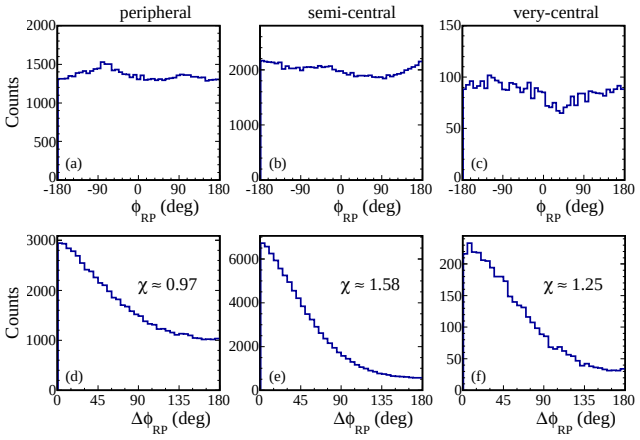

FIG. 10: (Top row) Inclusive distributions of the angle Φ_{RP} representing the reaction-plane orientation obtained with the Q-vector method from the combined CHIMERA and AToF data for peripheral (a), semicentral (b), and very central (c) impact-parameter intervals (see Table I for their definitions). (Bottom row) Distributions of the difference of orientations of the subevent reaction planes for the same three event classes, peripheral (d), semicentral (e), and very central (f), obtained with the mixing technique of Refs. [53, 54] and by using the weight $Z\beta_t\gamma$ (see text and Table II). The corresponding values of the reaction-plane dispersion parameter χ are indicated.

the location of the detector module that recorded the i^{th} hit. A minimum multiplicity of $N \geq 2$ was imposed. In this case, the weight factor ω has been omitted because the rapidity of the detected particles was not determined even though the Microball acceptance of $\theta_{\mathrm{lab}} \geq 60^\circ$ can be expected to select mainly backward emissions. As shown below, the orientation of $\vec{Q}_{\mu\mathrm{Ball}}$ was indeed found to be opposite to those of the CHIMERA and AToF Q vectors.

The three Q-vectors are strongly correlated. The degree of coincidence of the azimuthal orientations of the vectors $\vec{Q}_{\mathrm{CHI}}$ and $\vec{Q}_{\mathrm{AToF}}$ for the class of events containing a valid $\vec{Q}_{\mathrm{AToF}}$ is shown in Fig. 9. The individual reaction-plane orientations obtained from the CHIMERA and AToF Wall data are evidently very similar. With the target foil removed [panel (b)], the coincidence of orientations is no longer present; the correlation pattern is dominated by the slightly reduced acceptance of AToF in the region near 0°. The resulting distributions of the difference $\Phi_{\mathrm{CHI}} - \Phi_{\mathrm{AToF}}$ is shown in the bottom panel. The azimuthal angle Φ that is used here and in Figs. 10 and 11 is defined in accordance with the chosen coordinate system (Fig. 1), with $\Phi = 0^\circ$ coinciding with the x and $\Phi = 90^\circ$ with the y direction. The applied condition requiring that the CHIMERA and Microball orientations are within the adopted anticorrelation gate of $\pm 90^\circ$ suppresses unwanted background, as discussed in Sec. III D in more detail.

The inclusive reaction-plane distributions, as given by the combined Q-vectors obtained by summing over recorded hits in CHIMERA and AToF for three choices

of impact-parameter windows, are shown in the top row of Fig. 10. The observed flatness indicates that the particle angular distributions have not been biased by variations of the detector efficiencies, by properties of the event triggering or by other azimuthal asymmetries in the experiment.

Several different methods of estimating the reaction-plane orientation were applied to the data to identify possible systematic uncertainties related to it. They are all based on the Q-vector method of Ref. [51] but differ in the kinematic quantities used as weights for summing over the included particles and fragments. Besides the product $Z\beta_t\gamma$ [cf. Eq. (4)], equal weights for all particles and the atomic number Z alone of each particle were also used as weights for summing over the azimuthal directions of the recorded hits either in both CHIMERA and AToF or in CHIMERA alone. It was, in addition, investigated as to what extent the result varies with the value of the rapidity gate chosen for selecting the forward hemisphere in the c.m. reference frame.

Detectors and chosen weight	$y_{c.m.} > 0.1$	$y_{c.m.} > 0.2$
CHIMERA alone, equal weight	1.39	1.30
CHIMERA+AToF, equal weight	1.45	1.37
CHIMERA alone, Z	1.51	1.42
CHIMERA+AToF, Z	1.58	1.50
CHIMERA alone, $Z\beta_t\gamma$	1.52	1.42
CHIMERA+AToF, $Z\beta_t\gamma$	1.59	1.49

TABLE II: Resolution parameter χ obtained for the estimation of the reaction-plane orientation with different choices for the Q-vector construction for the case of semicentral ^{197}Au+^{197}Au collisions. The first column indicates the considered detector systems and weights; the second and third columns show χ for two values of the rapidity gate chosen for CHIMERA hits.

The criterion chosen for this investigation was the achieved resolution of the reaction-plane orientation. It determines the necessary corrections and the uncertainty associated with the obtained flow parameters [52]. It was evaluated with the subevent mixing technique as described in Refs. [53, 54] and quantified through the resolution parameter χ. This parameter is inversely proportional to the width of the difference distribution of subevent orientations, assumed to be Gaussian in the present case (cf. Ref. [52]). Examples of difference distributions obtained for selected intervals of impact parameter are given in the bottom row of Fig. 10, including the corresponding results for χ. The resolution parameters obtained with the studied choices of weights and detector systems are listed in Table II for the class of semicentral events. The best resolution, indicated by the largest value for χ, has been achieved using the product $Z\beta_t\gamma$ as the weight and by summing over the recorded hits with $y_{c.m.} > 0.1$ in both CHIMERA and AToF. All the results shown in the following sections were obtained with this choice. It is interesting to note, however, that other choices for the weighting factors lead to very comparable results (Table II).

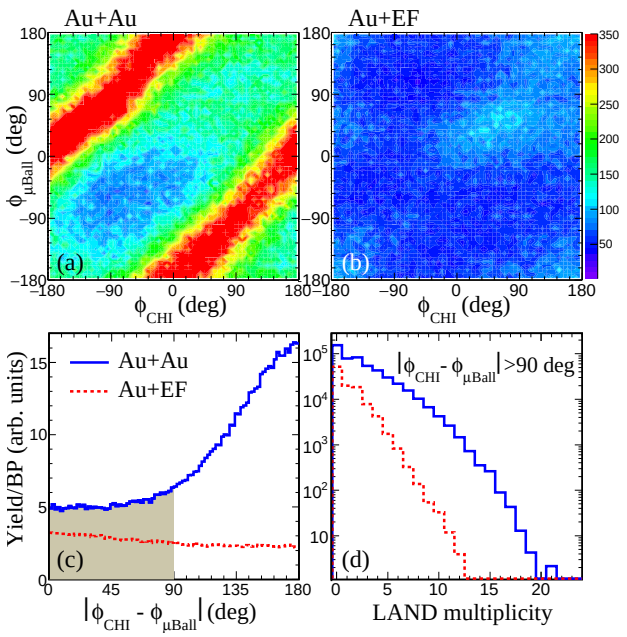

FIG. 11: (Top row) Correlation between the Q-vector orientations determined with CHIMERA (abscissa) and with the Microball (ordinate) for data sets taken with (a)) and without (b) a target foil in place (EF stands for empty frame). (Bottom row) Difference of the Q-vector orientations for Au+Au and for Au+EF data (c), normalized with respect to the integrated beam intensity (BP stands for beam particles), and the raw hit multiplicities (d) registered with LAND for Au+Au (solid line) and for Au+EF data sets (dotted line). The hatched area in (c) indicates the range of events rejected by the required anticorrelation of the CHIMERA and Microball Q-vector orientations (Sec. III D).

The correction factors resulting from the so determined dispersion of the reconstructed reaction plane were obtained according to Ref. [53, 54]. Resolution parameters χ in the range of 1.2 to 1.6 (Fig. 10) correspond to attenuation factors $\langle\cos(n\Delta\phi)\rangle$ of approximately 0.8 to 0.9 for $n = 1$, i.e., for the case of directed flow, and from ≈ 0.5 to 0.65 for the elliptic flow ($n = 2$). Their inverse values represent the correction factors to be applied to the Fourier coefficients describing the measured azimuthal anisotropies. The validity of the method used for determining the reaction-plane orientation and its experimental dispersion were confirmed by a comparison of collective flows obtained from the KRATTA and from FOPI data [48] for the same reaction. Excellent agreement is obtained for directed and elliptic flows of hydrogen and helium isotopes within the common acceptance of the two experiments [55].

D. Background corrections

For rejecting background reactions owing to the interaction of Au projectiles with non-target material,

the correlation of the Q-vector orientations as given by CHIMERA and by the Microball detectors was used. Figure 11 shows the correlation between their azimuthal directions, $\Phi_{\rm CHI}$ and $\Phi_{\mu\rm Ball}$, for ^{197}Au+^{197}Au reactions (a) and ^{197}Au+empty frame (b) data, normalized relative to each other with respect to the integrated beam intensities. The strong anticorrelation for on-target reactions is evident. It is expected because forward-emitted particles were selected with CHIMERA ($y_{\rm c.m.} > 0.1$) and the Microball covers mainly the backward hemisphere in the c.m. frame.

In runs with empty target frames, the recorded yields are low and only a weak positive correlation is observed. The distribution of differences between the two Q-vector orientations, normalized with respect to the integrated beam intensity, is presented in panel (c). To minimize the contributions of non-target collisions in the data analysis, an anticorrelation of the CHIMERA and Microball Q-vector orientations was required. The applied condition $|\Phi_{\rm CHI} - \Phi_{\mu\rm Ball}| > 90^\circ$ led to a relative weight of background reactions of less than 20%. It underlines the importance of the Microball data for identifying and rejecting off-target reactions.

Panel (d) of Fig. 11 shows the LAND raw multiplicity (number of modules hit per event), normalized with respect to the integrated beam intensity, for ^{197}Au+^{197}Au and ^{197}Au+empty frame data and after applying the CHIMERA-Microball anticorrelation condition. The contribution from non-target backgrounds in the kinematic region of LAND is weak, starting with less than 20% at unit multiplicity to much less than 1% at multiplicity 10. In the final analysis, normalized yields of the remaining non-target background events were subtracted from the corresponding ^{197}Au+^{197}Au data sets.

IV. EXPERIMENTAL RESULTS

Azimuthal distributions of neutrons and light-charged particles measured with LAND with respect to the reaction plane determined with the CHIMERA and AToF detectors, as described in the previous section, were extracted for ^{197}Au+^{197}Au reactions from data collected with and without a target and without and with the shadow bar in front of LAND. After subtracting the measured and normalized background yields, the obtained distributions were fitted with the Fourier expansion

$$f(\Delta\phi) \propto 1 + 2v_1\cos(\Delta\phi) + 2v_2\cos(2\Delta\phi) \qquad (6)$$

to determine the coefficients describing the observed directed (v_1) and elliptic (v_2) flows. $\Delta\phi$ represents the azimuthal angle of the momentum vector of an emitted particle with respect to the determined reaction plane [52]. Owing to insufficient resolution, charge identification with the ΔE-vs-time-of-flight technique has not been possible with LAND in the present experiment. Therefore, results only for neutrons and for all recorded charged particles are presented in the following.

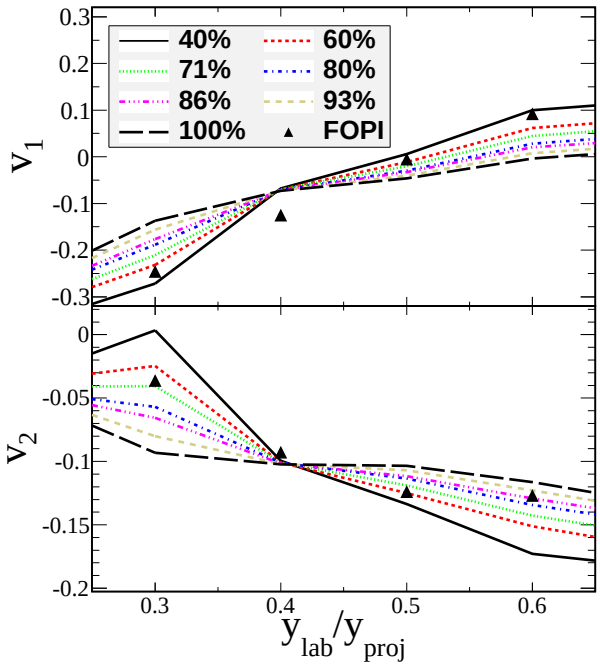

FIG. 12: Measured directed (top) and elliptic flows (bottom) of charged particles as determined with different timing corrections in comparison with FOPI results (solid triangles, from [48]) for the same ^{197}Au+^{197}Au reaction at 400 MeV/nucleon in the interval of impact parameters $3.35 \leq b \leq 6$ fm. The percentages of cases to which the so-called second step of the timing corrections was applied are given in the legend (see text). The solid and dashed black lines indicate the limits 40% and 100%, respectively, of the studied probability interval.

A. Timing corrections

The timing information of particles detected with LAND in these data sets had been corrected as described in Sec. III A and in the Appendix. One of the unknown parameters appearing in this procedure was the number of particles misplaced or wrongly corrected in the so-called second step. Therefore, a series of analysis runs was performed in which the percentage of particles subjected to it was reduced from 100% to 40% in steps of increasing width. The resulting flow parameters are shown in Fig. 12 as a function of the reduced rapidity $y_{\rm lab}/y_{\rm proj}$. It is observed that the influence of the second correction is negligible at rapidities $y_{\rm lab}/y_{\rm proj} \approx 0.4$ but significant at lower and higher rapidities. At a reduced rapidity $y_{\rm lab}/y_{\rm proj} = 0.4$, the acceptance of LAND in this experiment selects transverse momenta of approximately 0.3 to 0.5 GeV/c/nucleon for which the discussed effect is, apparently, less severe. As expected for a mixing between time intervals, the modifications at low and high rapidities occur in opposite directions for both the directed and the elliptic flows.

For the data selected for this purpose, an interval of nominal impact parameters $3.35 \leq b \leq 6$ fm was chosen

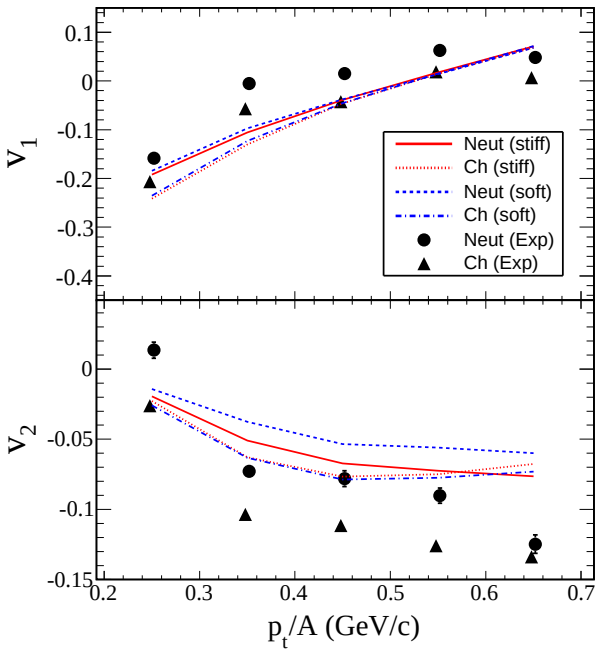

FIG. 13: Measured flow parameters v_1 (top) and v_2 (bottom) for the central event class ($b < 7.5$ fm) in ^{197}Au+^{197}Au collisions at 400 MeV/nucleon for neutrons (solid circles) and charged particles (solid triangles) as a function of the transverse momentum p_t/A. The UrQMD predictions for neutrons and charged particles obtained with a stiff (γ=1.5, red solid and dotted lines, respectively) and a soft (γ=0.5, blue dashed and dash-dotted lines, respectively) density dependence of the symmetry term have been filtered to correspond to the geometrical acceptance of the experiment. The experimental data are corrected for the dispersion of the reaction-plane orientation. Where not shown, the statistical errors are smaller than the size of the symbols.

because corresponding flow data have been made available by the FOPI Collaboration [48]. It is contained within the semicentral event class and its parameters are listed in the bottom line of Table I. The comparison is not meant to identify a "best" percentage at which the problem will largely disappear. It only shows that the 100% application of the second step does not necessarily lead to improved flow values, consistent with the observation made for the time spectra discussed in the Appendix. It also suggests an application with 40% as a useful lower limit. Variations within this interval of 40% to 100% are considered as suitable for quantifying the contribution of the mixing and the underlying timing uncertainty to the systematic error of the measurement. It applies mainly to the flow parameters deduced as a function of rapidity or of transverse momentum. The effect is of minor importance for the acceptance-integrated flow ratios based on time-integrated particle yields.

B. Collective flow

Flow parameters obtained after correcting for the dispersion of the reaction plane are shown in Fig. 13 as a function of the transverse momentum per particle p_t/A. They are integrated over the rapidity range covered by the LAND acceptance which increases with p_t/A from $y_{\rm lab}/y_{\rm proj} \approx 0.3$ to 0.7 (cf. Fig. 1 of Ref. [5]). The observed yield of particles decreases rapidly with increasing transverse momentum, so that the low-intensity regions at high p_t are more strongly affected by occasionally misplaced particles originating from the regions of high yield at lower p_t. For this reason, the analysis is restricted to transverse momenta $p_t/A \leq 0.7$ GeV/c. The selected range of nominal impact parameter is $b \leq 7.5$ fm (central event class), and a fraction of 80% is chosen for the application of the second correction step discussed above, compatible with the comparison of elliptic-flow results shown in Fig. 12. The coefficient v_1 rises from negative values for small p_t/A to small positive values at $p_t/A > 0.6$, reflecting the correlation of transverse momentum with rapidity caused by the acceptance of LAND. The coefficient v_2 is small at small p_t/A and assumes values below $v_2 = -0.1$ at larger p_t/A, indicating the strength of particle squeeze-out in the directions perpendicular to the reaction plane.

V. INTERPRETATION WITH URQMD

As in the earlier FOPI-LAND study [5], the ultrarelativistic QMD (UrQMD) model of the group of Li and Bleicher [9–11] has been employed to deduce the density dependence of the nuclear symmetry energy. Even though alternative parametrizations have recently become available [56, 57], the version employed in the FOPI-LAND study was used again, so as to permit a direct comparison of the density dependencies obtained from the two experiments. The differences are, furthermore, not very large. In the study presented by Wang *et al.* using a variety of Skyrme forces a very comparable stiffness parameter $L = 89 \pm 23$ MeV was obtained, differing from the original result $L = 83 \pm 26$ MeV by only a few MeV [5, 57]. The parameter

$$L = 3\rho_0 \frac{\partial E_{\rm sym}}{\partial \rho}|_{\rho=\rho_0} \qquad (7)$$

is proportional to the slope of the symmetry energy at saturation (see, e.g., Ref. [38]).

The UrQMD model was originally developed to study particle production at high energy [58]. By introducing a nuclear mean field with momentum-dependent forces, it has been adapted to the study of intermediate-energy heavy-ion collisions [59]. The chosen equation of state is soft. The updated Pauli-blocking scheme, introduced to provide a more precise description of experimental observables at lower energies, is described in Ref. [60]. Different options for the dependence on isospin asymmetry

were implemented. Two of them are used here, expressed as a power-law dependence of the potential part of the symmetry energy on the nuclear density ρ according to

$$E_{\rm sym} = E_{\rm sym}^{\rm pot} + E_{\rm sym}^{\rm kin} = 22\,{\rm MeV}(\rho/\rho_0)^{\gamma} + 12\,{\rm MeV}(\rho/\rho_0)^{2/3}, \quad (8)$$

with $\gamma = 0.5$ and $\gamma = 1.5$ corresponding to a soft and a stiff density dependence.

The UrQMD predictions for these two choices are shown in Fig. 13 in comparison with the experimental data for both neutrons and charged particles. A filtering procedure was used to adapt the results to the experimental conditions. They qualitatively follow the experimental flow values, even though the predicted squeeze-out is less pronounced than that observed. A significant sensitivity with respect to the stiffness of the symmetry energy is visible for the elliptic flow of neutrons. By comparing it to the strength of the charged-particle flow in the form of flow ratios or differences, this sensitivity is expected to be preserved, even in the presence of a global over- or underprediction of the elliptic flows [5, 6].

The slight underprediction is known to be related to the so-called FP1 parametrization for the momentum dependence of the elastic nucleon-nucleon cross sections in the default version of the UrQMD model that was used here. UrQMD studies of the reaction dynamics at intermediate energies have shown that the in-medium modification of the elastic nucleon-nucleon cross-sections is an important ingredient for realistic descriptions, and various parametrizations have been tested [56]. In the previous FOPI-LAND study, additional calculations were performed with the FP2 parametrization, causing the elliptic-flow parameter v_2 to be slightly overpredicted. The absolute values of v_2 obtained with FP1 and FP2 differ by $\approx 40\%$ for this reaction [60, 61]. The calculated ratios retain, nevertheless, the sensitivity of the elliptic flow to the stiffness of the symmetry energy and depend only weakly on the chosen parametrization for the in-medium cross sections [5].

The systematic study of the residual model dependence of transport descriptions of the elliptic-flow ratios and differences by Cozma *et al.* [14] has, in addition, demonstrated that the Tübingen QMD transport model used there leads to equivalent results regarding the deduced stiffness of the symmetry energy. In particular, also the impact of including or neglecting the momentum dependence of the symmetry potential was investigated with different parametrizations. Important input quantities identified by this study were the isoscalar compressibility and the width of the nucleon wave function employed in the calculations. Narrower constraints for these quantities will reduce the theoretical uncertainties. A quantitative study of the model differences between the UrQMD and the Tübingen versions was performed by Wang *et al.* [57]. Expressed in terms of the central value obtained for the slope parameter L, an uncertainty of $\Delta L \approx 10$ MeV may be ascribed to the observed model dependence of the UrQMD versus the Tübingen-QMD analyses.

Besides the momentum-dependence of the symmetry potential [16, 62–66], attention has to be paid to the recent observation of short-range correlations [67, 68], leading to larger tails of the momentum distributions in symmetric matter than in pure neutron matter and to a reduction of the kinetic part in the parametrization of the symmetry energy [69–71]. It will be interesting to incorporate these correlations in transport models and to explore their consequences [72, 73]. However, in a first study [29], the effect for elliptic-flow ratios was found to be negligibly small for the case of a mildly soft to linear density dependence of the symmetry energy that is supported by the present data. It is, nevertheless, evident that the improvement of current theoretical descriptions is an important goal for the future. Reducing theoretical uncertainties and enhancing their consistency [74], will permit tighter constraints for the high-density dependence of the symmetry energy.

The UrQMD transport program is stopped at a collision time of 150 fm/c and a conventional phase-space coalescence model with two parameters is used to construct clusters. Nucleons with relative momenta smaller than P_0 and relative distances smaller than R_0 are considered as belonging to the same cluster. The values $P_0 = 0.275$ GeV/c and $R_0 = 3.0$ fm have been adopted as standard parameters. With these values the overall dependence of cluster yields on Z is rather well reproduced but the yields of $Z = 2$ particles are underpredicted [5]. In the comparison with the FOPI data set used for Fig. 12, after normalization with respect to $Z = 1$, an underprediction by a factor 1.4 was observed. The yields of deuterons and tritons in central collisions are also underestimated by similar factors.

Constraints for the symmetry energy were determined by comparing the ratios of the elliptic flows of neutrons and charged particles (ch), v_2^n/v_2^{ch}, with the corresponding UrQMD predictions for the soft and stiff assumptions. Because hydrogen isotopes could not be selected, as done in the FOPI-LAND study [5], a test was performed for confirming the equivalence of results obtained when including all recorded charged particles in the analysis. For this purpose, the data of the FOPI-LAND experiment were analyzed with and without the condition $Z = 1$ applied in the charged-particle selection and with the limitation $p_t/A \leq 0.7$ GeV/c of the integration interval in transverse momentum. The corresponding power-law coefficients γ were determined by comparing with UrQMD calculations performed with the same conditions. In addition, the effect of enhancing the weight of the $Z = 2$ contribution to the calculated Z-integrated flow was tested. Because good agreement was obtained with an enhancement factor 1.4, corresponding to the observed underprediction, it was used as default option in the analysis. Overall, the changes observed in these tests for the central values were less than $\Delta\gamma = 0.05$, accompanied however by the larger statistical error of the FOPI-LAND data set.

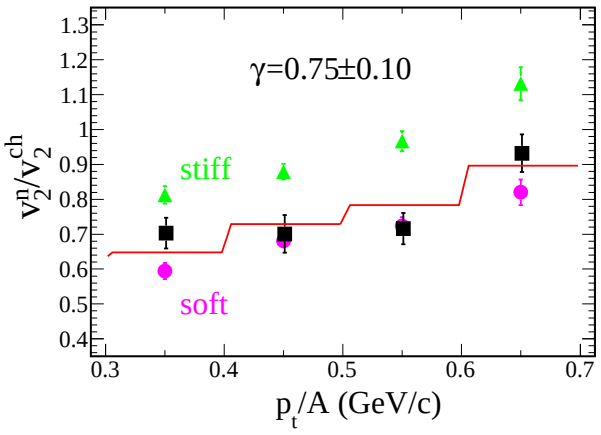

FIG. 14: Elliptic flow ratio of neutrons over all charged particles for central ($b < 7.5$ fm) collisions of ^{197}Au+^{197}Au at 400 MeV/nucleon as a function of the transverse momentum per nucleon p_t/A, evaluated with a fraction of 80% for the second step of timing corrections (see Sec. IV A). The black squares represent the experimental data; the green triangles and purple circles represent the UrQMD predictions for stiff ($\gamma = 1.5$) and soft ($\gamma = 0.5$) power-law exponents of the potential term, respectively. The solid line is the result of a linear interpolation between the predictions, weighted according to the experimental errors of the included four bins in p_t/A and leading to the indicated $\gamma = 0.75 \pm 0.10$.

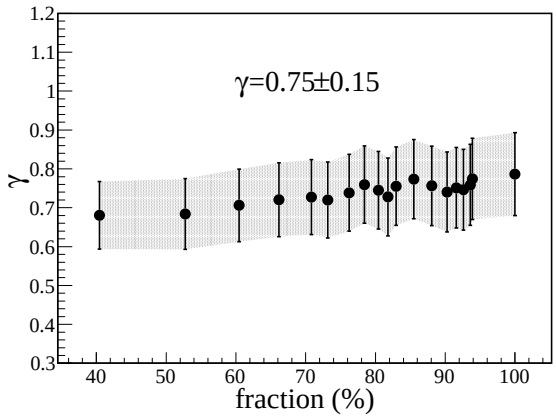

FIG. 15: Potential-term coefficient γ deduced by interpolating between the UrQMD predictions shown in Fig. 14 as a function of the fraction chosen for the second step of timing corrections (see Sec. IV A).

A. Differential data

The ratio v_2^n/v_2^{ch} obtained from the present data for the class of central ($b < 7.5$ fm) collisions as a function of the transverse momentum per nucleon p_t/A is shown in Fig. 14. The chosen fraction for the second step of timing corrections (see Sec. IV A) is 80%, compatible with the comparison with FOPI data presented in Fig. 12. Under this assumption, the best description of the neutron-vs-charged-particle elliptic flow is obtained with a power-law coefficient $\gamma = 0.75 \pm 0.10$, where $\Delta\gamma = 0.10$ is the statistical uncertainty returned by the fit routine. It results from linearly interpolating between the predictions for the soft, $\gamma = 0.5$, and the stiff, $\gamma = 1.5$, predictions of the model within the range of transverse momentum $0.3 \leq p_t/A \leq 0.7$ GeV/c.

The dependence of the resulting γ on the choice made for the second timing correction in the data analysis is shown in Fig. 15. Under the assumption that the second correction should be applied to at least 40% of the corresponding particles, the 1-σ error margins are confined within the interval $\gamma = 0.75 \pm 0.15$ as apparent from the figure. The larger error $\Delta\gamma = 0.15$ is expected to include the systematic uncertainty caused by the existence of misplaced hits, not identified in the first step and only partly included in the second step of the timing correction scheme of the analysis.

B. Acceptance-integrated flow ratio

The new constraint deduced in the preceding section is slightly lower but still within the uncertainty interval of the previous value $\gamma = 0.9 \pm 0.4$ deduced from the FOPI-LAND data and the same UrQMD model [5]. The error is significantly reduced by a factor of more than two. To confirm the validity of the obtained result and to minimize complications arising from the time-of-flight measurement with LAND, an acceptance-integrated flow ratio was determined by integrating over the full $t_{\rm hit}$ spectrum shown in Fig. 21 in the Appendix. It includes all recorded particles irrespective of their actual location within this spectrum. The corresponding UrQMD calculations were integrated over the full acceptance of LAND as given by the covered interval of laboratory angles. The thresholds and the energy and particle-type dependent detection efficiency of the effectively used first plane of the LAND detector behind the veto wall were taken into account (Fig. 16). The efficiency calculations were carried out with Geant3 within the FairRoot software framework [47].

The still remaining uncertainty arising from this procedure is connected with the choice of the upper limit of the time-of-flight interval which determines the lower threshold of the neutron energy. For protons to pass through the veto wall and to be detected in a LAND module, a minimum energy of about 60 MeV is required while neutrons with lower energies may still be detected (Fig. 16). The magnitude of this effect has been assessed by varying the upper limit of time-of-flight integration between 60 and 90 ns, resulting in a slight variation of the obtained flow ratio and the exponent γ. The UrQMD calculations were performed for this purpose with kinetic-energy thresholds that corresponded to the chosen integration limit for neutrons and the physical lower detection thresholds for charged particles. Acceptance-

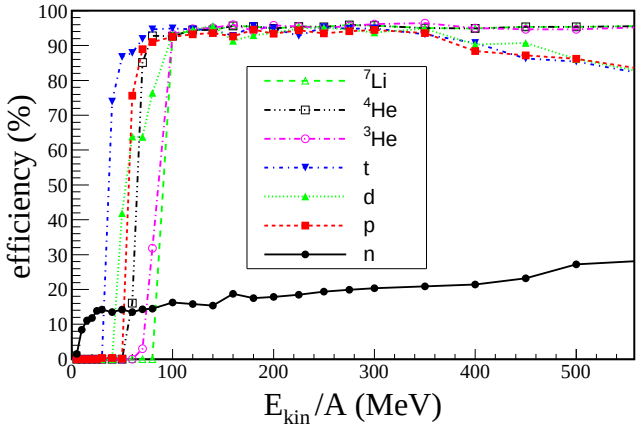

FIG. 16: Detection probability of the first plane of the LAND detector, preceded by the veto wall, for neutrons (dots), protons (solid squares), deuterons (solid triangles), tritons (solid tip-down triangles), ^{3}He (open circles), ^{4}He (open squares), and ^{7}Li (open triangles) as a function of the particle kinetic energy per nucleon $E_{\rm kin}/A$.

integrated elliptic-flow values were then determined from the azimuthal anisotropy of the obtained yields and the linear interpolation between the predictions was used to determine the corresponding exponents γ.

The results for the measured and calculated acceptance-integrated flow ratios and the resulting γ are shown in Fig. 17. A small monotonic variation of γ with the assumption regarding the upper limit of the ToF interval is evident. The 1-σ error margins are confined to the interval $\gamma = 0.77 \pm 0.17$. It overlaps with the interval obtained by varying the fraction of hits included in the second correction step (Fig. 15). This is not unexpected as the two methods are both aiming at quantifying the remaining consequences of not recognized simultaneous timing errors of the two signals from a paddle. The variation of the maximum of the ToF interval, in addition, includes the effect of a possible smearing of the energy threshold for neutrons and charged particles by the 25-ns time jumps.

C. Final corrections

Up to this point, the effects of charge-changing processes, nuclear or instrumental, have been ignored in the analysis. The largest effects of this kind are caused by misidentifications of charged particles as neutrons, because of a missing veto signal, and of neutrons as charged particles because of a neutron-induced reaction in a veto panel that produces a signal. Nuclear charge-exchange reactions with cross sections on the level of millibarn are less important in comparison (see, e.g., Refs. [75, 76]). Furthermore, protons converted into neutrons in the veto wall may still have left a signal there while neutrons converted to protons are included in the measured, rather small, efficiency for neutron detection of the thin veto

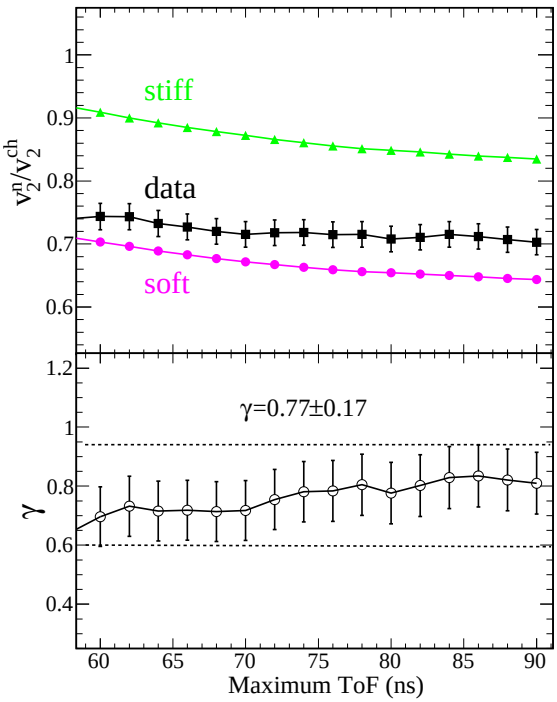

FIG. 17: Measured elliptic-flow ratio for central ($b < 7.5$ fm) collisions of ^{197}Au+^{197}Au at 400 MeV/nucleon in comparison with stiff and soft UrQMD predictions (top) and deduced symmetry term coefficient γ (bottom) as a function of the upper limit of the time-of-flight interval used to obtain time integrated results. The dashed horizontal lines mark the upper and lower limits of the 1-σ statistical error margin $\Delta\gamma = \pm 0.10$ within the time interval $60 < ToF < 90$ ns.

paddles (see below). Misidentifications reduce the difference between the measured flow patterns and thus cause a small increase of the apparent flow ratio. The resulting symmetry-term coefficient appears stiffer than without these effects.

Calculations within the R3BRoot simulation framework [47] have been performed with different assumptions regarding the detector response and particle recognition. In particular, the particle-dependent detection thresholds have been taken into account (Fig. 16). The obtained reduction of the power-law exponent γ varied between $\Delta\gamma = -0.03$ and -0.07, with the lower and upper boundaries being obtained with the most extreme assumptions.

The magnitude of the required correction is, qualitatively, easily understood. A 1-mm gap between veto paddles causes an inefficiency of approximately 1%. It may cause the equivalent amount of charged particles to appear as neutrons in the analysis. As charged particles by nature, they have a five-fold higher probability for being detected in the first layer of LAND. By taking into account the known yield ratio of charged particles over neutrons of approximately 2/3 and the measured flow ratio of $v_2^n/v_2^{ch} = 0.72$ (Fig. 17), a corrected ratio $v_2^n/v_2^{ch} = 0.71$ is obtained. With the sensitivity of

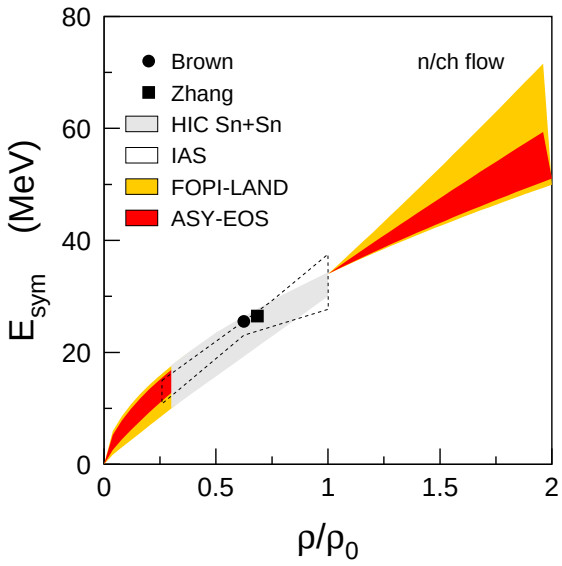

FIG. 18: Constraints deduced for the density dependence of the symmetry energy from the present data in comparison with the FOPI-LAND result of Ref. [5] as a function of the reduced density ρ/ρ_0. The low-density results of Refs. [78–81] as reported in Ref. [82] are given by the symbols, the gray area (HIC), and the dashed contour (IAS). For clarity, the FOPI-LAND and ASY-EOS results are not displayed in the interval $0.3 < \rho/\rho_0 < 1.0$.

the flow ratio as represented in the figure, the correction amounts to $\Delta\gamma = -0.05$. It represents an upper limit for this particular effect because the veto paddles are aligned with respect to the elements of the first plane of LAND and not all particles passing through the veto gaps are recorded. As an analysis detail, we note here that in testing the coincidence of timing signals in the veto wall and first plane of LAND the possibility of undetected ±25-ns displacements of one of the signals was taken into account (errors in the positions derived from the time signals have all been corrected, see Appendix). Other processes exist but are less important. The detection probability for neutrons in the 5-mm veto paddles is below 1% (cf. Fig. 1 of Ref. [17]) and the coincidence requirement of a matching hit in the first module of LAND further reduces the probability of misidentifications of this kind. In the simulations, all these effects are included.

The adopted reduction $\Delta\gamma = -0.05 \pm 0.02$ leads to a final result for the power-law coefficient $\gamma = 0.72 \pm 0.19$. The quoted uncertainty is obtained by a linear addition of the systematic error of the correction and the $\Delta\gamma = -0.17$ uncertainty resulting from the comparison of the acceptance-integrated flow ratio with the UrQMD calculations (Fig. 17). The possibility of charge misidentifications considered here has not been taken into account in the FOPI-LAND analysis. There its magnitude appears small in comparison with the uncertainty $\Delta\gamma = \pm 0.4$ of this earlier result. It was also not included yet in presentations of preliminary ASY-EOS results at conferences [77].

The obtained constraint for the density dependence of the symmetry energy is shown in Fig. 18 in comparison with the FOPI-LAND result of Ref. [5] as a function of the reduced density ρ/ρ_0. The new result confirms the former and has a considerably smaller uncertainty. Judging from the purely statistical error of $\Delta\gamma = \pm 0.10$ (Fig. 14), even smaller errors can be expected from future measurements.

For reference, the low-density behavior of the symmetry energy from Refs. [78–81] as reported in Ref. [82] is included in the figure. The present parametrization is found compatible also with these results from nuclear structure studies and from reactions at lower bombarding energy. The corresponding slope parameter describing the variation of the symmetry energy with density at saturation is $L = 72 \pm 13$ MeV. Judging from the analysis work done with the FOPI-LAND data, one may expect that the analysis of the present data with the Tübingen QMD [6, 14] will lead to a similar or possibly slightly larger value for the parameter L [15, 57, 83].

The sharp value $E_{\rm sym}(\rho_0) = 34$ MeV is a consequence of the chosen parametrization [Eq. (8)]. Using values lower than the default $E^{\rm pot}_{\rm sym}(\rho_0) = 22$ MeV, as occasionally done in other UrQMD studies [56, 84], is likely to lower the result for L. Values of the symmetry energy at saturation in the interval between 30 MeV and 32 MeV seem to be favored by a majority of terrestrial experiments and astrophysical observations as shown in recent compilations [85, 86]. Motivated by these results, the present UrQMD analysis has, in addition, been performed with $E^{\rm pot}_{\rm sym}(\rho_0) = 19$ MeV, corresponding to $E_{\rm sym}(\rho_0) = 31$ MeV. The obtained power-law coefficient $\gamma = 0.68 \pm 0.19$ is lower by $\Delta\gamma = 0.04$ and the corresponding slope parameter $L = 63 \pm 11$ MeV is lower by 9 MeV, changes that both remain within the error margins of these quantities. It is to be noted, however, that the precise results of Brown [80] and Zhang and Chen [81] are no longer met with this alternative parametrization of the symmetry energy.

VI. DENSITY PROBED

Calculations predict that central densities of two to three times the saturation density may be reached in ^{197}Au+^{197}Au collisions at 400 to 1000 MeV/nucleon on time scales of $\approx 10 - 20$ fm/c [87]. The resulting pressure produces a collective outward motion of the compressed material whose strength, differentiating between neutrons and protons, is influenced by the symmetry energy in asymmetric systems [25]. It is to be expected, however, that the observed transverse momenta of emitted particles and their azimuthal variation apparent as elliptic flow carry information acquired during the full reaction history. The tests performed with the FOPI-LAND flow data and varying parameters for the potential part of the symmetry energy in the UrQMD had already

indicated that densities above and below saturation contribute to the observed flow patterns [5].

A force-weighted density has been defined by Le Fèvre *et al.* in their recent study of the equation of state of symmetric matter, based on FOPI elliptic-flow data and IQMD calculations [24]. For ^{197}Au+^{197}Au collisions at 400 MeV/nucleon, its broad maximum extends over densities $0.8 < \rho/\rho_0 < 1.6$. Liu *et al.* report in their study of pion production in the same reaction that the relative sensitivity of the π^-/π^+ yield ratios to the symmetry energy is distributed over a density range of approximately $0.7 < \rho/\rho_0 < 1.8$ with a maximum near $\rho/\rho_0 \approx 1.2$ [88]. These more quantitative studies, with partly different methods, consistently support the assumption that suprasaturation densities up to nearly twice saturation are probed at this energy with collective flows and meson production, not exclusively but with major effects produced above saturation.

For the present purpose, a detailed analysis of the collision processes has been performed with the Tübingen version [14] of the QMD model (TüQMD). The sensitivity to the various density regimes probed in heavy-ion collisions was studied quantitatively by examining their impact on the variation of elliptical-flow-ratio observables with the two choices of a mildly stiff and a soft parametrization for the density-dependent asymmetric-matter equation of state (asy-EoS). To that end, the density-dependent quantity DEFR (difference of elliptic-flow ratio)

$$\mathrm{DEFR}^{(n,Y)}(\rho) = \frac{v_2^n}{v_2^Y}(x=-1,\rho) - \frac{v_2^n}{v_2^Y}(x=1,\rho) \qquad (9)$$

has been determined using the TüQMD transport model. Here Y labels a particle or a group of particle species and x the asy-EoS stiffness resulting from the momentum-dependent one-body potential introduced by Das *et al.* [16]. The density-dependent elliptic-flow ratios (EFR) in this expression are calculated with a modified symmetry potential

$$V_{\mathrm{sym}}(x,\tilde{\rho}) = \begin{cases} V_{\mathrm{sym}}^{\mathrm{Gogny}}(x,\tilde{\rho}) & \tilde{\rho} \le \rho \\ V_{\mathrm{sym}}^{\mathrm{Gogny}}(0,\tilde{\rho}) & \tilde{\rho} > \rho \end{cases} \qquad (10)$$

with $x = \pm 1$ according to Eq. (9). The difference of the $x = \pm 1$ potentials is tested only at densities up to the particular ρ, the argument of DEFR. This choice leads to $\mathrm{DEFR}^{(n,Y)}(0) = 0$ and to the proper stiff-soft splitting for large values of the density ρ. Values at intermediate densities are a measure of the impact on elliptic flow observables of regions of density lower than that chosen for the argument. The derivative of DEFR with respect to density provides thus the sensitivity density of the elliptic flow ratio observable under consideration as a function of the nuclear matter density.

In the top panel of Fig. 19, the density dependence of $\mathrm{DEFR}^{(n,Y)}$ for the choice Y=all charged particles (ch) is presented. It is seen that DEFR increases monotonically up to density values in the neighborhood of $2.5\,\rho_0$, close to the maximum density probed by nucleons in heavy-ion collisions at 400 MeV/nucleon incident energy. The relative sensitivity of the elliptic flow ratio of neutrons over charged particles to the various density regions is presented in the bottom panel of Fig. 19, together with the same quantity for the neutron-over-proton and neutron-over-hydrogen flow ratios. It is readily observed that the maximum sensitivity of the neutron/proton EFR lies in the 1.4 to 1.5 ρ_0 region. It is lowered to 1.0 to 1.1 ρ_0 for the choices that involve light complex particles. The probed regions of nuclear density are thus considerably higher than the densities around or below 0.7 ρ_0 probed with nuclear structure observables [80–82]. Even lower densities in the vicinity of $\rho_0/3$ have very recently been reported as the region of sensitivity probed with the dipole polarizability of ^{208}Pb [89].

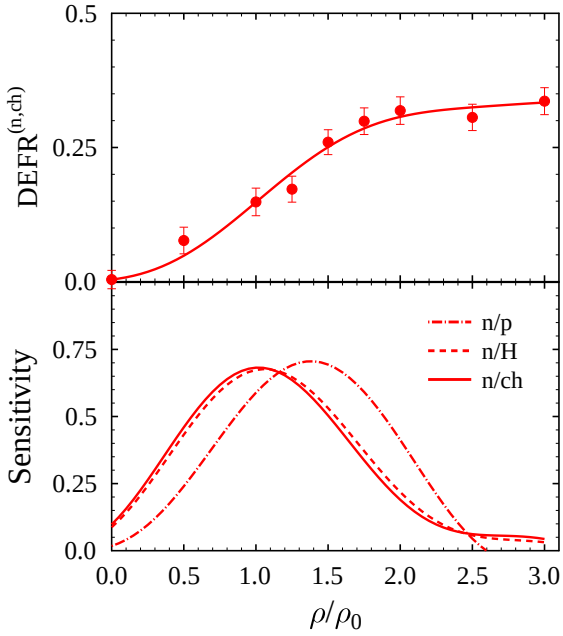

FIG. 19: Density dependence of the difference of the elliptic flow ratio (DEFR) of neutrons over charged particles, defined by Eq. (9), for ^{197}Au+^{197}Au collisions at 400 MeV/nucleon obtained with the TüQMD transport model [14] and the FOPI-LAND acceptance filter (top) and the corresponding sensitivity density (bottom, solid line) together with sensitivity densities obtained from elliptic-flow ratios of neutrons over all hydrogen isotopes (dashed line) and neutrons over protons (dash-dotted line).

The moderately different density regions probed by EFR observables involving protons and, respectively, light complex particles are expected to lead to slightly different extracted values for the asy-EoS stiffness. Preliminary results, employing existing experimental FOPI-LAND data for v_2^n/v_2^p and v_2^n/v_2^H and the TüQMD transport model, suggest this to be the case [90]. A slightly stiffer asy-EoS is favored by the latter observable, a difference that will be enhanced if one corrects for the fact that transport models coupled with phase-space coalescence algorithms tend to underpredict light cluster mul-

tiplicities by factors ranging up to 2-3. Deuterons and tritons are of particular interest here. This result suggests that, at higher densities, the asy-EoS density dependence is somewhat softer than at saturation. It may thus be feasible to extract constraints for the parameters of the higher-order terms of the Taylor expansion of the symmetry energy in density around the saturation point, in particular the curvature parameter $K_{\rm sym}$. Information regarding the curvature is of high interest as, e.g., the inclusion of exchange terms in microscopic models cause a stiffening [91], while considering the momentum tails caused by short-range correlations may cause a softening [73] of the predictions for the symmetry energy in the density regime near and above saturation.

It is, therefore, of extreme importance for future experiments to be able to extract a clean separate proton signal. Additionally, theoretical models that allow for an independent adjustment of the slope and curvature parameters of the symmetry energy term will be required to be able to push the extracted constraints for the asy-EoS density dependence into the $2\rho_0$ region.

VII. CONCLUSION AND OUTLOOK

From the measurement of the elliptic flows of neutrons and light charged particles in the reaction ^{197}Au+^{197}Au at 400 MeV/nucleon incident energy a new, more stringent constraint for the nuclear symmetry energy at suprasaturation density has been deduced. From the comparison of the elliptic flow ratio of neutrons over charged particles with UrQMD predictions, a value $\gamma = 0.72 \pm 0.19$ is obtained for the power-law coefficient of the potential part in the parametrization of the model. It confirms the moderately soft to linear density dependence of the symmetry energy deduced previously from the FOPI-LAND data. The densities probed were shown to reach beyond twice saturation.

The effects of deficiencies of the LAND timing electronics have been studied in detail and their effects assessed by systematically varying correction parameters over their intervals of uncertainty. An acceptance-integrated flow ratio for neutrons over charged particles has been generated by integrating over the time-of-flight spectra. It is largely insensitive to timing uncertainties but still subject to a systematic error caused by an instrumental smearing of detection thresholds. Their effect contributes to the total error $\Delta\gamma = \pm 0.19$ of the acceptance-integrated result that includes a statistical error $\Delta\gamma = \pm 0.10$.

The slope parameter that corresponds to the obtained parametrization of the symmetry energy is $L = 72 \pm 13$ MeV. As densities near and beyond saturation are efficiently probed with the present observable, one may convert this result into a symmetry pressure $p_0 = \rho_0 L/3 = 3.8 \pm 0.7$ MeVfm^{-3} (with $\rho_0 = 0.16$ fm^{-3}), equivalent to $6.1 \pm 1.1 \times 10^{32}$ Pa. It represents the pressure in pure neutron matter at saturation because the pressure in symmetric matter vanishes at this density. The pressure in neutron-star matter with asymmetries $\delta = (\rho_n - \rho_p)/\rho$ less than unity should be lower. The estimate developed in Sec. 9.1 of Ref. [38], based on β equilibrium, yields a proton fraction $x_p = (1-\delta)/2$ of about 5% for $E_{\rm sym} = 34$ MeV [cf. Eq. (8)] and saturation density. With the corresponding asymmetry $\delta = 0.90$, the pressure of the asymmetric baryonic matter is reduced to 3.1 MeVfm^{-3}. Adding the contribution of the degenerate electrons yields a value of 3.4 MeVfm^{-3} for the pressure in neutron-star matter at saturation density. The same or very similar values are obtained with the expressions presented in Refs. [86, 92]. Compared to the results of Steiner *et al.* [93], they are located within the upper half of the 95% confidence interval obtained by these authors from neutron-star observations.

While interpretations in this direction may still appear speculative at present and in need of further study, they reveal the potential of pressure measurements in nuclear reactions. As far as the modeling of nuclear reactions is concerned, it will be important to improve the description of the nuclear interaction in transport models [74], reduce the parameter ranges also in the isoscalar sector, improve the algorithms used for clusterization, as well as go beyond the mean-field picture, including short-range correlations. The latter have recently been investigated in nuclei [67, 68] and their consequences for transport descriptions of intermediate-energy heavy-ion reactions are of high interest and need to be investigated [72]. Moreover, it will be quite important to compare the experimental data with the predictions of several transport models, of both Boltzmann-Vlasov and molecular-dynamics type [94], to pursue the work towards a model-independent constraint of the high-density symmetry energy initiated in Ref. [14].

The results of the present experiment, together with the theoretical study of the density probed, may also be seen as a strong encouragement for extending the measurement of neutron and charged particle flows to other reaction systems and energies. The presented calculations suggest that the curvature parameter $K_{\rm sym}$ can be addressed experimentally if higher precision and elemental and isotopic resolution for charged particles can be achieved. Future experiments will, therefore, benefit from the improved calorimetric capabilities of the NeuLAND detector presently constructed as part of the R^3B experimental setup [95] and from the availability of radioactive ion beams for reaction studies at FAIR.

Acknowledgments

The authors are indebted to the Accelerator Department and the Target Laboratory of the GSI Helmholtzzentrum for providing high-quality beams and targets. We are particularly grateful to the Laboratori Nazionali del Sud for making parts of the CHIMERA multidetector available for the experiment. We thank

W. Reisdorf and the FOPI Collaboration for providing specifically selected data sets from their experiments and for continuing support of the project. The contributions of R. Bassini and C. Boiano during the preparatory phase are gratefully acknowledged.

This work has been supported by the European Union under Contract No. FP7-25431 (Hadron-Physics2), by INFN (Istituto Nazionale di Fisica Nucleare) experiments EXOCHIM and NEWCHIM, by the National Natural Science Foundation of China under Grants No. 11375062, No. 11547312, and No. 11505057, by the Hungarian OTKA Foundation No. K106035, by the Polish Ministry of Science and Higher Education under Grant No. DPN/N108/GSI/2009, by the Foundation for Polish Science - MPD program, co-financed by the European Union within the European Regional Development Fund, by the Polish National Science Center (NCN), Contracts No. UMO-2013/10/M/ST2/00624 and No. UMO-2013/09/B/ST2/04064, by the Slovak Scientific Grant Agency under Contract 2/0121/14, by the UK Science and Technology Facilities Council (STFC) under Grants No. ST/G008833/1, No. ST/I003398/1, and No. STBA00019, by the U.S. Department of Energy under Grants No. DE-FG02-93ER40773 and No. de-sc0004835, by the U.S. National Science Foundation Grant No. PHY-1102511, and by the Robert A. Welch Foundation through Grant No. A-1266.

VIII. APPENDIX: CORRECTION OF LAND TIMING

In the TACQUILA electronic board [43], the time measurement of a recorded hit is performed by registering the time of the start signal (tac) inside a 25-ns clock-cycle window, the time of the common stop signal inside its 25-ns clock-cycle window (so-called t_{17}), and the number n_c of cycles occurring between the start and stop cycles. The returned calibrated time information $t_{\rm cal}$ is then given by

$$t_{\rm cal} = {\rm tac} + 25n_c - t_{17}\ ({\rm ns}). \tag{11}$$

The resolution of the timing system is of the order of 10 ps (rms) [43].

Examples of the observed correlations between t_{17} (in channels) and the so measured $t_{\rm cal}$ (in ns) for the two photomultipliers (PM's) of a paddle of the first plane of LAND are shown in panels (a) and (b) of Fig. 20, respectively. Ideally, no correlation should be visible as the distribution of the stop signals inside the clock cycle window should be completely random. Unexpectedly, however, a strong correlation is observed; preferences exist, primarily, for high t_{17} values at smaller times $t_{\rm cal}$ but also for low t_{17} values at larger times. This behavior by itself implies an improper functioning of the TACQUILA board. It is evidence of incorrect determinations of n_c, depending on where the t_{17} signal appears within the clock cycle. In addition, it was found that the probability of wrong n_c countings was rate dependent; it increased with increasing frequency of hits recorded in the LAND modules. This behavior, as discovered during the data taking was confirmed with bench tests performed after the experiment and ultimately corrected by replacing parts of the TACQUILA electronic readout system.

As a consequence, the region marked as A1 in Fig. 20 (a) must be considered as overpopulated because of a wrong counting of the number n_c of clock cycles; the returned n_c is likely to be one unit smaller than the true value, causing an offset of -25 ns of the calibrated time $t_{\rm cal}$. With smaller probability, counting errors larger than one cycle were observed as well. It follows that any measured time in LAND is not necessarily but possibly wrong by ± 25 ns or, with decreasing probability, even multiples of it.

The described malfunctions clearly affect the measurements of the hit position $Y_{\rm time}$ along the vertically oriented paddles, derived from the difference, and of the arrival time $t_{\rm hit}$ at the paddle, derived from the sum of the two signals recorded for a hit. The two quantities are given by

$$Y_{\rm time} = t_{\rm cal_1} - t_{\rm cal_2} \tag{12}$$

$$t_{\rm hit} = (t_{\rm cal_1} + t_{\rm cal_2})/2 \tag{13}$$

where the indices 1 and 2 refer to the two PM's of a given paddle; the signals $t_{\rm cal_1}$ and $t_{\rm cal_2}$ are, at this stage, not yet synchronized, i.e. not yet corrected for time offsets generated by, e.g., differences of the cable lengths of the two PMs. The position $Y_{\rm time}$ is, therefore, still given in units of nanoseconds and not necessarily centered with respect to the paddle length.

In the case of malfunctions, the time differences may be sufficiently large, so that the deduced hit position falls outside the physical length of the paddle. This can be easily corrected by adding or subtracting 25 ns to the time difference. It will move the hit to its correct position inside the paddle. To recover the correct arrival times $t_{\rm hit}$ is not equally feasible in this case. It would require the knowledge of whether the wrong position of $Y_{\rm time}$ is caused by erroneous +25 ns in one or -25 ns in the other of the two signals coming from a paddle. The two possibilities correspond to $t_{\rm hit}$ values that differ by 25 ns. Moreover, it is also possible that both time measurements are affected by the same ± 25 ns time jump. In that case, the position $Y_{\rm time}$ is correct but the returned arrival time $t_{\rm hit}$ is erroneous by ± 25 ns. Because the expected range of arrival times at LAND exceeds 25 ns, an easy and straightforward procedure for recovering the correct time information does not exist.

It has, nevertheless, been possible to develop a correction scheme for recovering the correct times with high probability and for determining the consequences of remaining uncertainties for the finally determined symmetry-term coefficient. This was achieved with the help of correction parameters whose effects can be as-

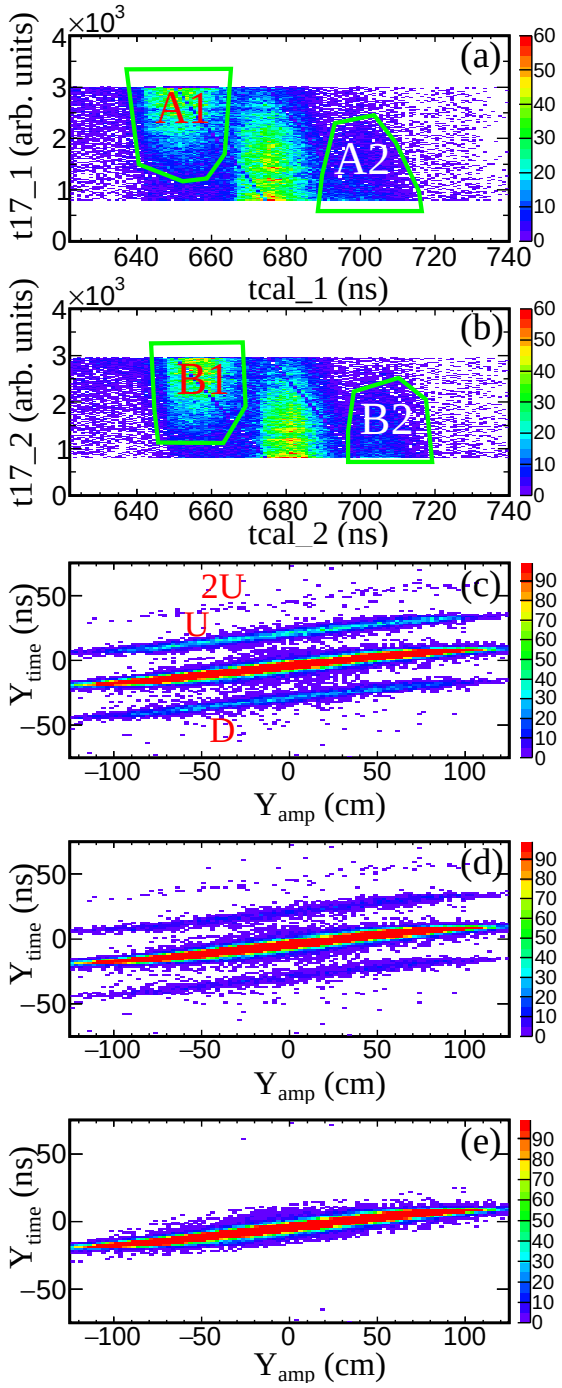

FIG. 20: (a),(b) Observed correlations of t_{17} vs calibrated time $t_{\rm cal}$ for the two signals $t_{\rm cal_1}$ and $t_{\rm cal_2}$ of a module of the first plane of LAND, respectively. (c),(d) Observed correlations of the position signals $Y_{\rm time}$ vs $Y_{\rm amp}$ deduced from the time and amplitude information of these signals, respectively, before (c) and after (d) the first correction step. (e) the same correlation after the correction step 1^{st}bis. The significance of the marked regions in panels (a) through (c) is explained in the text.

sessed on a quantitative level. The scheme divides into two parts.

The first correction step starts from the observed correlation of the position measurement $Y_{\rm time}$ with the position $Y_{\rm amp}$ obtained from the amplitudes of the normalized PM signals. The uncorrected correlation [Fig. 20(c)] shows clearly separated regions of unphysical positions $Y_{\rm time}$, marked with U (up), D (down), and 2U (twice up), in addition to the strongest group of coinciding position measurements. The distribution of uncorrected positions $Y_{\rm time}$ for a typical module of the first plane of LAND is shown in the top panel of Fig. 21 and the corresponding $t_{\rm hit}$ distribution is shown in the bottom panel of the same figure ("no corr," solid line in black). The two side groups with wrong $Y_{\rm time}$ positions are weak ($< 10\%$) compared to the main group but significant. The probability for double time jumps in the same direction is below 1% and essentially negligible. The 25-ns repetitions of structures in $t_{\rm hit}$ are clearly visible in Fig. 21 (bottom panel), in particular, the repeated appearance of narrow artificial peaks generated by the electronics. These structures were removed before other corrections were applied.

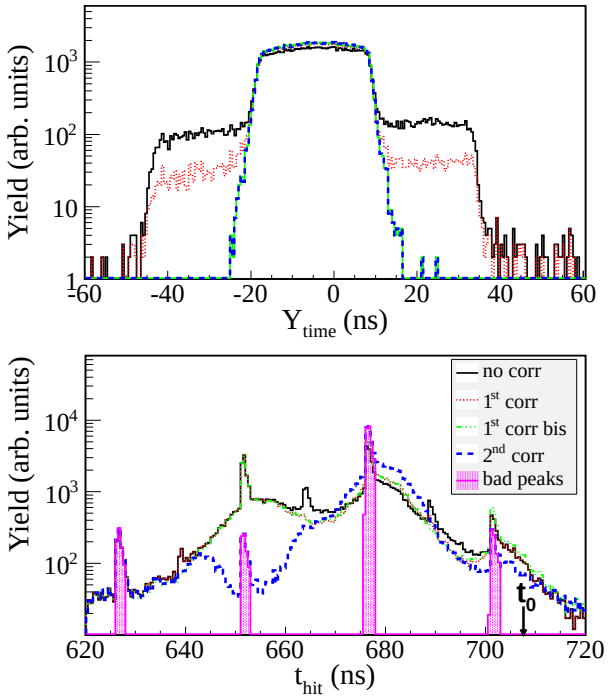

FIG. 21: Hit distributions for a module of the first plane of LAND as a function of the position $Y_{\rm time}$ (top) and of the arrival time $t_{\rm hit}$ (bottom). Black solid lines denote the uncorrected distributions, the colored lines represent the distributions after the 1^{st} (red, small dots), the 1^{st}bis (green, thick dots), and the 2^{nd} (blue, thick dashed) corrections. "Bad peaks" refers to artificial sharp peaks at 25 ns intervals (solid purple areas) generated by the electronic readout.

In the attempt to correct the wrong positions, the chosen scheme takes into account the value of t_{17} relative to the returned time as shown in panels (a) and (b) of

Fig. 20. In the example of a hit belonging to the region 'U' in panel (c), $t_{\mathrm{cal_1}}$ may be located in what is defined as the "good" region, i.e., in the interval between 640 ns and 720 ns but outside the gates 'A1' and 'A2' in panel (a), and $t_{\mathrm{cal_2}}$ may be located in region 'B1' of panel (b). In this case, it is obviously more probable that $t_{\mathrm{cal_2}}$ is incorrect, i.e., that the number of clock cycles is wrong by one unit, and 25 ns are thus added to its value. Instead, if $t_{\mathrm{cal_1}}$ is located in region 'A2' and $t_{\mathrm{cal_2}}$ in the "good" region, i.e, outside the gates 'B1' and 'B2' in panel (b), 25 ns are subtracted from $t_{\mathrm{cal_1}}$. Corresponding corrections are applied to hits belonging to regions marked as 'D' and '2U' in Fig. 20(c), as well as to a region '2D' when it appeared in other cases. This part of the correction scheme is summarized in Table III and marked as 1^{st} step in the last column. Note that three possibilities exist for correcting the rare double jumps, depending on where the hits are found to be located. The superscripts "+" and "-" used in the table indicate regions analogous to the four regions 'A1', 'A2', 'B1', and 'B2' marked in panels (a) and (b) of Fig. 20 but located further out by another +25 ns or -25 ns from the central part of the spectrum.

panel (c)	panel (a)	panel (b)	$t_{\mathrm{cal_1}}$	$t_{\mathrm{cal_2}}$	correction
U	A2		-25 ns		1^{st}
U		B1		+25 ns	1^{st}
D	A1		+25 ns		1^{st}
D		B2		-25 ns	1^{st}
2U	A2	B1	-25 ns	+25 ns	1^{st}
2U	$A2^{+}$		-50 ns		1^{st}
2U		$B1^{-}$		+50 ns	1^{st}
2D	A1	B2	+25 ns	-25 ns	1^{st}
2D	$A1^{-}$		+50 ns		1^{st}
2D		$B2^{+}$		-50 ns	1^{st}
good	A1	B1	+25 ns	+25 ns	2^{nd}
good	A2	B2	-25 ns	-25 ns	2^{nd}

TABLE III: The first three columns indicate the regions referred to in the listed panels of Fig. 20 while the next two columns specify the actions taken on $t_{\mathrm{cal_1}}$, $t_{\mathrm{cal_2}}$, or both. The last column indicates the number of the correction step as given in the text.

Panel (d) of Fig. 20 shows the Y_{time}-vs-Y_{amp} correlation after this first correction step. The corresponding Y_{time} and t_{hit} distributions are shown in Fig. 21 (in red). It is evident that not all the wrong positions have disappeared because some hits do not fulfill the assumptions made in devising the first step of the correction scheme (of the order of 2%, cf. Fig. 21, top panel). In that case, an additional correction called 1^{st}bis is applied. At this step, the location of the hit pattern in the t_{17}-vs-t_{cal} maps [Figs. 20(a) and 20(b)] is ignored and the correct Y_{time} is recovered by either adding 25 ns to one or by subtracting 25 ns from the other of the two time signals $t_{\mathrm{cal_1}}$ and $t_{\mathrm{cal_2}}$ of that hit. The choice made between these two possibilities was based upon which of them had appeared with the higher probability when the 1^{st} correction step had been applied to the same paddle. Panel (e) of Fig. 20 shows the Y_{time}-vs-Y_{amp} correlation after this correction: Now all the positions deduced from time signals are correct. They coincide with the positions deduced from the amplitudes and are within the physical length of the paddle (Fig. 21, top, in green, coinciding with blue).

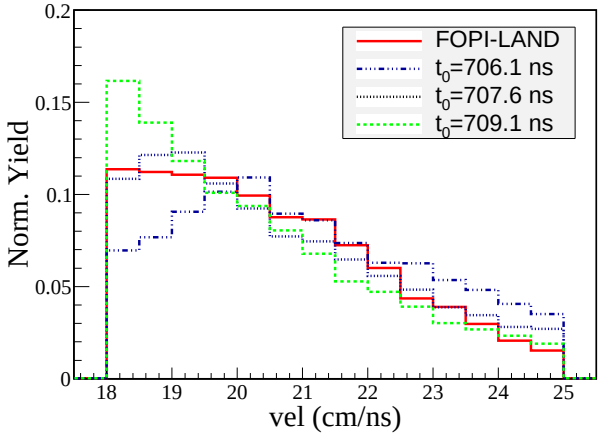

FIG. 22: High velocity tail of normalized velocity spectra for several assumptions on the time-zero value t_0 in comparison with the corresponding spectrum measured in the FOPI-LAND experiment.

At this stage, cases in which both time measurements are affected by the same time jump have not been touched. They remain correct regarding their positions Y_{time} but the problem of their erroneous arrival times t_{hit} is not solved yet. For that purpose, an additional correction step has been conceived. It is based on the assumption that the coincident location of the two signals of a hit in either regions 'A1' and 'B1' or in 'A2' and 'B2' of their respective t_{17}-vs-t_{cal} maps is a strong indication of a simultaneous jump. The correction step consists of either adding or subtracting 25 ns to both values $t_{\mathrm{cal_1}}$ and $t_{\mathrm{cal_2}}$ of that hit, so that they fall into the central regions of their maps. It is marked as 2^{nd} step in the last column of Table III. It simply changes the arrival times t_{hit} by 25 ns but leaves the position Y_{time} and its correlation with Y_{amp} unaffected. The so-obtained final t_{hit} distribution is shown in Fig. 21 (bottom panel, in blue).

It is evident that the second correction step falsely modifies correctly measured cases of long or short times with time signals $t_{\mathrm{cal_1}}$ and $t_{\mathrm{cal_2}}$ accidentally falling into the marked regions. Its effect is particularly large in the interval 640 to 660 ns of the t_{hit} spectrum, where it causes a depression (Fig. 21, bottom panel). The geometric mean between the yields before and after this correction would approximately represent a smooth time spectrum that would seem more probable. This level can be reached if only about 80% of the hits near the center down to about 50% towards the edges of this region are actually moved in the second step, while the rest of the selected candidates are left at their original arrival times in the 640 ns-to-660 ns interval. However, as it is

not known which of the hits should be moved and which should be left at their time positions, a correction of this kind is not properly feasible. It will smoothen the time spectrum but, because of the necessarily random selection, an inevitable mixing of hits between the affected time intervals will occur.

This situation was addressed by considering the fraction of randomly selected hits whose arrival times are actually modified in step 2 as an unknown correction parameter. The time spectrum in Fig. 21 (bottom panel) and the comparison of flow results as a function of this fraction with FOPI results (Fig. 12 in Sec. IV A) suggest a value of at least 40%. Apart from that, it remains unknown and its significance for the differential flow ratios must be assessed. The result, a systematic variation of $\Delta\gamma = 0.05$ as a function of this fraction, is shown in Fig. 15 and discussed in Sec. V A. For the acceptance-integrated analysis based on time-integrated data sets (Sec. V B), the present corrections are of minor importance because very few hits are actually moved across the boundaries of the integration interval.

Owing to the logarithmic gain chosen for the new TACQUILA electronic board, the signals of low-energy γ rays fell below threshold with the effect that the calibration of the time spectra could not be based on a measured γ peak. The location of the zero-time-of-flight point t_0 was, therefore, determined from a comparison of velocity spectra, generated with various assumptions on t_0, with the well-calibrated spectrum available from the FOPI-LAND experiment. The high-velocity part of the spectrum was found to exhibit the most distinctive variation as a function of the choice for t_0 (Fig. 22). The presence of artificial peaks at arrival times $t_{\rm hit} \approx 677$ and 702 ns (Fig. 21, bottom panel) limited the useful range to velocities $vel > 18$ cm/ns or $E_{\rm kin} > 230$ MeV for nucleons. The rapid variation of the velocity spectrum with the choice of t_0 permitted its determination with an uncertainty of the order of 1 ns (Fig. 22). Its location at $t_{\rm hit} = 707.6$ ns is marked in the spectrum of arrival times $t_{\rm hit}$. As the displayed times are measured with respect to a delayed common stop signal, finite time-of-flight values are to the left of t_0. Photons would appear at $t_{\rm hit} = 691$ ns, indicating that the yield at larger $t_{\rm hit}$ represents the level of background and of hits that are still misplaced. The interval $18 \leq vel < 25$ cm/ns used for the comparison corresponds to $680 \leq t_{\rm hit} < 688$ ns, a region only mildly affected by corrections. The same is true for the main group of recorded hits with arrival times between $t_{\rm hit} = 669$ and 685 ns, corresponding to flight times between 23 and 39 ns and to kinetic energies of 100 to 400 MeV for nucleons (note that artificial peaks are removed).

The correction effects are stronger for arrival times between $t_{\rm hit} = 642$ and 663 ns, expected for nucleons with approximately 30 to 70 MeV kinetic energy. The time spectrum in that region is strongly modified by the second correction step moving particles from this region into the main group centered at $t_{\rm hit} = 680$ ns (Fig. 21, bottom panel). The threshold energy of 60 MeV for protons to pass through the veto wall and to be detected in a LAND module is located within the affected region ($t_{\rm hit} = 659$ ns). The same is true for the thresholds of deuterons and tritons, located at smaller energy per nucleon and correspondingly longer times of flight.

To be independent of the applied corrections, the acceptance-integrated result was obtained by integrating the time spectra up to $t_{\rm hit} = 640$ ns, i.e., beyond the critical regions. The maximum time of flight of 67.5 ns defines a threshold of 30 MeV for neutrons. It is lower than the physical thresholds for charged particles, a condition that was equally applied in the UrQMD simulations. Only double time jumps and background events, apart from the neutrons below threshold, can contribute to the low-intensity region at $t_{\rm hit} < 640$ ns. Possible systematic effects related to these effects were investigated by varying the integration limit between $617 < t_{\rm hit} < 648$ ns, i.e., flight times between 60 and 90 ns, and by correspondingly adjusting the neutron-energy threshold in the calculations. The resulting variation of γ is small as shown in Fig. 17.

It is once more noted here that the timing corrections are applied to all particles independently of whether they are charged or neutral. This has obviously reduced their influence on the flow ratios that are used as the principal observables, in agreement with the results of the tests performed.

[1] Bao-An Li, Zhongzhou Ren, C. M. Ko, and S. J. Yennello, Phys. Rev. Lett. **76**, 4492 (1996).
[2] Bao-An Li, Phys. Rev. Lett. **88**, 192701 (2002).
[3] V. Greco, V. Baran, M. Colonna, M. Di Toro, T. Gaitanos, and H. H. Wolter, Phys. Lett. **B 562**, 215 (2003).
[4] Gao-Chan Yong, Bao-An Li, and Lie-Wen Chen, Phys. Rev. C **74**, 064617 (2006).
[5] P. Russotto *et al.*, Phys. Lett. **B 697**, 471 (2011).
[6] M. D. Cozma, Phys. Lett. **B 700**, 139 (2011).
[7] Y. Leifels *et al.*, Phys. Rev. Lett. **71**, 963 (1993).
[8] D. Lambrecht *et al.*, Z. Phys. **A 350**, 115 (1994).
[9] Qingfeng Li, Zhuxia Li, S. Soff, R. K. Gupta, M. Bleicher, and H. Stöcker, J. Phys. **G 31**, 1359 (2005).
[10] Q. Li, Z. Li, S. Soff, M. Bleicher, and H. Stöcker, J. Phys. G **32**, 151 (2006).
[11] Q. Li, Z. Li, S. Soff, M. Bleicher, H. Stöcker, J. Phys. G **32**, 407 (2006).
[12] D. T. Khoa, N. Ohtsuka, M. A. Matin, A. Faessler, S. W. Huang, E. Lehmann, and R. K. Puri, Nucl. Phys. **A 548**, 102 (1992).
[13] V. S. Uma Maheswari, C. Fuchs, A. Faessler, L. Sehn, D. S. Kosov, and Z. Wang, Nucl. Phys. **A 628**, 669 (1998).
[14] M. D. Cozma, Y. Leifels, W. Trautmann, Q. Li, and

P. Russotto, Phys. Rev. C **88**, 044912 (2013).
[15] P. Russotto, M. D. Cozma, A. Le Fèvre, Y. Leifels, R. Lemmon, Q. Li, J. Łukasik, and W. Trautmann, Eur. Phys. Jour. A **50**:38 (2014).
[16] C. B. Das, S. D. Gupta, C. Gale and B.-A. Li, Phys. Rev. C **67**, 034611 (2003).
[17] Th. Blaich *et al.*, Nucl. Instr. and Meth. **A 314**, 136 (1992).
[18] A. Pagano *et al.*, Nucl. Phys. **A 734**, 504 (2004).
[19] E. De Filippo and A. Pagano, Eur. Phys. Jour. A **50**:32 (2014).
[20] A. Schüttauf *et al.*, Nucl. Phys. **A 607**, 457 (1996).
[21] D. G. Sarantites *et al.*, Nucl. Instr. and Meth. **A 381**, 418 (1996).
[22] J. Łukasik *et al.*, Nucl. Instr. and Meth. **A 709**, 120 (2013).
[23] W. Reisdorf *et al.*, Nucl. Phys. **A 876**, 1 (2012).
[24] A. Le Fèvre, Y. Leifels, W. Reisdorf, J. Aichelin, and Ch. Hartnack, Nucl. Phys. **A 945**, 112 (2016).
[25] P. Danielewicz, R. Lacey, and W. G. Lynch, Science **298**, 1592 (2002).
[26] W. Reisdorf *et al.*, Nucl. Phys. **A 781**, 459 (2007).
[27] Jun Hong and P. Danielewicz, Phys. Rev. C **90**, 024605 (2014).
[28] T. Song and C. M. Ko, Phys. Rev. C **91**, 014901 (2015).
[29] Gao-Chan Yong, Phys. Rev. C **93**, 044610 (2016).
[30] Bao-An Li, Phys. Rev. C **92**, 034603 (2015).
[31] Wen-Mei Guo, Gao-Chan Yong, and Wei Zuo, Phys. Rev. C **92**, 054619 (2015).
[32] M. D. Cozma, Phys. Lett. **B 753**, 166 (2016).
[33] Zhigang Xiao, Bao-An Li, Lie-Wen Chen, Gao-Chan Yong, and Ming Zhang, Phys. Rev. Lett. **102**, 062502 (2009).
[34] Zhao-Qing Feng and Gen-Ming Jin, Phys. Lett. **B 683**, 140 (2010).
[35] W.-J. Xie, J. Su, L. Zhu, and F.-S. Zhang, Phys. Lett. **B 718**, 1510 (2013).
[36] V. Baran, M. Colonna, V. Greco, M. Di Toro, Phys. Rep. **410**, 335 (2005).
[37] J.M. Lattimer and M. Prakash, Phys. Rep. **442**, 109 (2007).
[38] Bao-An Li, Lie-Wen Chen, Che Ming Ko, Phys. Rep. **464**, 113 (2008).
[39] M. Di Toro, V. Baran, M. Colonna, V. Greco, J. Phys. G **37**, 083101 (2010).
[40] S. Gandolfi, A. Gezerlis, J. Carlson, Annu. Rev. Nucl. Part. Sci. **65**, 303 (2015).
[41] W. Trautmann and H.H. Wolter, Int. J. Mod. Phys. E **21**, 1230003 (2012).
[42] Topical Issue on Nuclear Symmetry Energy, Eur. Phys. Jour. A **50**, number 2 (2014).
[43] K. Koch *et al.*, IEEE Trans. Nucl. Sci. **52**, 745 (2005).
[44] G. Pasquali *et al.*, Nucl. Instr. and Meth. **A 301**, 101 (1991).
[45] L. Acosta *et al.*, IEEE Trans. on Nucl. Sci **60**, 284 (2013).
[46] R. Ogul *et al.*, Phys. Rev. C **83**, 024608 (2011).
[47] http://fairroot.gsi.de/.
[48] W. Reisdorf, priv. comm. (2013).
[49] W. Trautmann *et al.*, Phys. Rev. C **76**, 064606 (2007).
[50] J. Hubele, *et al.*, Z. Phys. A **340**, 263 (1991).
[51] P. Danielewicz and G. Odyniec, Phys. Lett. **B 157**, 146 (1985).
[52] A. Andronic, J. Łukasik, W. Reisdorf, and W. Trautmann, Eur. Phys. J. **A 30**, 31 (2006).
[53] J.-Y. Ollitrault, preprint nucl-ex/9711003 (1997).
[54] J.-Y. Ollitrault, Nucl. Phys. **A 638**, 195c (1998).
[55] S. Kupny, J. Brzychczyk, J. Łukasik, P. Pawłowski *et al.*, in *Proceedings of IWM-EC 2014, International Workshop on Multi facets of EoS and Clustering, Catania, Italy, 2014, edited by B. Borderie, R. Bougault, A. Pagano, S. Pirrone, and G. Politi*, EPJ Web of Conferences 88, 01010 (2015).
[56] Y. Wang, C. Guo, Q. Li, H. Zhang, Z. Li, and W. Trautmann, Phys. Rev. C **89**, 034606 (2014).
[57] Y. Wang, C. Guo, Q. Li, H. Zhang, Y. Leifels, and W. Trautmann, Phys. Rev. C **89**, 044603 (2014).
[58] S. A. Bass *et al.*, Progr. Part. Nucl. Phys. **41**, 255 (1998).
[59] Q. Li and M. Bleicher, J. Phys. G **36**, 015111 (2009).
[60] Qingfeng Li, C. Shen, C. Guo, Y. Wang, Z. Li, J. Łukasik, W. Trautmann, Phys. Rev. C **83**, 044617 (2011).
[61] Qingfeng Li, Caiwan Shen, and M. Di Toro, Mod. Phys. Lett. A **25**, 669 (2010).
[62] Bao-An Li, C. B. Das, S. Das Gupta, and C. Gale, Phys. Rev. C **69**, 011603(R) (2004).
[63] V. Giordano, M. Colonna, M. Di Toro, V. Greco, and J. Rizzo, Phys. Rev. C **81**, 044611 (2010).
[64] Zhao-Qing Feng, Nucl. Phys. **A 878**, 3 (2012).
[65] Lei Zhang, Yuan Gao, Yun Du, Guang-Hua Zuo, and Gao-Chan Yong, Eur. Phys. J. **A 48**: 30 (2012).
[66] Wen-Jie Xie, Zhao-Qing Feng, Jun Su, and Feng-Shou Zhang, Phys. Rev. C **91**, 054609 (2015).
[67] R. Subedi *et al.*, Science **320**, 1476 (2008).
[68] O. Hen *et al.*, Science **346**, 614 (2014).
[69] A. Carbone, A. Polls, and A. Rios, Europhysics Letters **97**, 22001 (2012).
[70] A. Rios, A. Polls, and W. H. Dickhoff, Phys. Rev. C **89**, 044303 (2014).
[71] Bao-An Li, Wen-Jun Guo, Zhaozhong Shi, Phys. Rev. C **91**, 044601 (2015).
[72] Or Hen, Bao-An Li, Wen-Jun Guo, L. B. Weinstein, and Eli Piasetzki, Phys. Rev. C **91**, 025803 (2015).
[73] Bao-Jun Cai and Bao-An Li, Phys. Rev. C **93**, 014619 (2016).
[74] Jun Xu *et al.*, Phys. Rev. C **93**, 044609 (2016).
[75] B. D. Anderson, L. A. C. Garcia, D. J. Millener, D. M. Manley, A. R. Baldwin, A. Fazely, R. Madey, N. Tamimi, J. W. Watson, and C. C. Foster, Phys. Rev. C **54**, 237 (1996).
[76] I. Tanihata *et al.*, preprint arXiv:1512.00590 [nucl-ex] (2015).
[77] P. Russotto *et al.*, in *Proceedings of IWM-EC 2014, International Workshop on Multi facets of EoS and Clustering, Catania, Italy, 2014, edited by B. Borderie, R. Bougault, A. Pagano, S. Pirrone, and G. Politi*, EPJ Web of Conferences 88, 00022 (2015).
[78] M. B. Tsang, Y. Zhang, P. Danielewicz, M. Famiano, Z. Li, W. G. Lynch, and A. W. Steiner, Phys. Rev. Lett. **102**, 122701 (2009).
[79] P. Danielewicz and J. Lee, Nucl. Phys. **A 922**, 1 (2014).
[80] B. A. Brown, Phys. Rev. Lett. **111**, 232502 (2013).
[81] Z. Zhang and L. W. Chen, Phys. Lett. **B 726**, 234 (2013).
[82] C. J. Horowitz, E. F. Brown, Y. Kim, W. G. Lynch, R. Michaels, A. Ono, J. Piekarewicz, M. B. Tsang, and H. H. Wolter, J. Phys. **G 41**, 093001 (2014).
[83] W. Trautmann, PoS Bormio2014, 036 (2014).
[84] Y. Wang, C. Guo, Q. Li, H. Zhang, Sci. China Phys. Mech. Astron. **55**, 2407 (2012).
[85] Bao-An Li and Xiao Han, Phys. Lett. **B 727**, 276 (2013).

[86] J. M. Lattimer and A. W. Steiner, Eur. Phys. J. **A 50**: 40 (2014).
[87] Bao-An Li, Nucl. Phys. **A 708** (2002) 365.
[88] He-lei Liu, Gao-Chan Yong, and De-Hua Wen, Phys. Rev. **C 91**, 044609 (2015).
[89] Zhen Zhang and Lie-Wen Chen, Phys. Rev. C **92**, 031301(R) (2015).
[90] M. D. Cozma, preliminary results and private communication (2015).
[91] V. Greco, M. Colonna, M. Di Toro, G. Fabbri, and F. Matera, Phys. Rev. C **64**, 045203 (2004).
[92] J. M. Lattimer and M. Prakash, Astrophys. J. **550**, 426 (2001).
[93] A. W. Steiner, J. M. Lattimer, and E. F. Brown, Astrophys. J. Lett. **765**, 5 (2013).
[94] Wen-Mei Guo, Gao-Chan Yong, Yongjia Wang, Qingfeng Li, Hongfei Zhang, and Wei Zuo, Phys. Lett. **B 738**, 397 (2014).
[95] https://www.gsi.de/r3b.